Atmospheric Research 273 (2022) 106174

Contents lists available at ScienceDirect

Atmospheric Research

journal homepage: www.elsevier.com/locate/atmosres

GPM-CO observations of Medicane Ianos: Comparative analysis of precipitation structure between development and mature phase

Leo Pio D'Adderio, Daniele Casella, Stefano Dietrich, Paolo Sanò, Giulia Panegrossi *

National Research Council of Italy, Institute of Atmospheric Sciences and Climate (CNR-ISAC), Rome, Italy

ARTICLE INFO

Keywords:
Tropical-like cyclone
Medicane Ianos
Remote sensing
GPM
Mediterranean storms
GMI
DPR

ABSTRACT

The present work exploits the satellite measurements from the NASA/JAXA Global Precipitation Measurement Core Observatory (GPM-CO) active and passive microwave sensors to analyze the precipitation structure of the most intense Mediterranean Hurricane (Medicane) on record, named Ianos, which swept across the Ionian Sea between 14 and 18 September 2020. Two GPM-CO overpasses, available during Ianos development and tropical-like cyclone (mature) phase, are analyzed in detail. GPM Microwave Imager measurements are used to carry out a comparative analysis of the medicane precipitation structure and microphysics processes between the two phases. The GPM-CO Dual-frequency Precipitation Radar overpass, available for the first time during a medicane mature phase, provides key measurements and products to analyze the 3D precipitation structure in the rainbands, offering further evidence of the main precipitation microphysics processes inferred from the passive microwave measurement analysis. Substantial difference in the rainband precipitation structure is observed, with deeper convection and stronger updraft features during development than at the mature phase, when also shallow precipitation/warm rain processes are observed in the inner region around the medicane eye. These features play a key role to explain the substantial drop in lightning activity during Ianos mature phase. Graupel-ice electrification process is inhibited due to the combined effect of strong horizontal wind and the observed limited growth of graupel. The study demonstrates the value of the GPM-CO not only to characterize Medicane Ianos precipitation structure and microphysics processes with unprecedented detail, but also to provide evidence of its exceptional intensity, tropical-like characteristics during its mature phase, and its similarities with tropical cyclones.

1. Introduction

Mediterranean hurricanes (Medicanes) or tropical-like cyclones (TLCs), are meso-scale cyclones typical of the Mediterranean area which share some dynamical features with the tropical cyclones, even if they are smaller in size, during their mature stage (i.e., at their maximum intensity): the presence of a quasi-cloud-free calm eye, spiral-like cloud bands elongated from the center, strong winds close to the vortex center and a deep warm core (Lagouvardos et al., 1999; Miglietta et al., 2013, 2015; Miglietta and Rotunno, 2019). Medicanes are often associated to heavy rainfall and flooding, intense wind, and high waves and storm surge, and can be serious threats to human life and infrastructure (Michaelides et al., 2018; Moscatello et al., 2008; Reale, 2001). These cyclones may last for several days, although the presence of tropical-like characteristics, showing a typical diameter of 100–300 km and associated surface wind speed that can occasionally reach 80–100 km/h, is generally limited to a few hours. In the mature stage, they may develop an axi-symmetric structure with vertical alignment of pressure minima, weak vertical wind shear and a warm core anomaly generally due to the release of latent heat associated with convection developing around the pressure minimum. The vertical extension of the warm core varies from the lower to the upper troposphere (Lagouvardos et al., 1999; Picornell et al., 2014; Ragone et al., 2018), and characterizes the duration of the tropical-like phase (as also evidenced by Emanuel (2005)). Miglietta et al. (2017) link the warm core vertical structure to the lower and upper level Potential Vorticity (PV) anomalies associated to medicane, in particular to dry PV, associated with the intrusion of stratospheric dry air, and wet PV generated by latent heat release due to condensation. Such latent heat release at low levels would extend to upper levels only in case of long lasting cyclones. Other authors have speculated that in some cases the warm core of medicanes would be the result of a warm air seclusion in the cyclone core (Fita and Flaounas, 2018; Mazza et al.,

* Corresponding author.
E-mail address: g.panegrossi@isac.cnr.it (G. Panegrossi).

https://doi.org/10.1016/j.atmosres.2022.106174
Received 27 October 2021; Received in revised form 3 March 2022; Accepted 2 April 2022
Available online 6 April 2022

2017). Miglietta and Rotunno (2019) have proposed to distinguish the latter category of cyclones from those with tropical-like characteristics. Medicanes are generally considered as quite rare events, and some studies have explored their frequency using models or observations (Cavicchia et al., 2014; Miglietta et al., 2013; Nastos et al., 2018). In particular, Cavicchia et al. (2014) obtained a systematic and homogeneous statistics of medicanes, over a six-decade period, and estimated an occurrence of about 1.5 medicanes per year, with large inter-annual variability and maximum occurrence during the fall and winter season.

Several studies have investigated the origin of medicanes and the main mechanisms for their development, intensification and transition to their mature phase with tropical-like characteristics by using both observations and models (Davolio et al., 2009; Emanuel, 2005; Flaounas et al., 2021; Miglietta et al., 2011; Miglietta and Rotunno, 2019; Pytharoulis et al., 1999; Reale, 2001). There has been a long-term and active debate on whether medicanes can be considered purely diabatic systems as tropical cyclones, and to what extent the different mechanisms, linked to both extra-tropical and tropical cyclone theory, are responsible for their development (e.g., Emanuel, 2005; Miglietta and Rotunno, 2019; Flaounas et al., 2021). In early studies, their intensification and maintenance within a pre-existing organized cyclonic environment were attributed mainly to sea surface energy fluxes (Wind-Induced Surface Heat Exchange (WISHE), Emanuel (1986)) enhanced by the contrast between cold air and relatively warmer sea surface. Since medicanes originate in baroclinic environments, generally associated with an upper-level cold trough (or a cut-off low), baroclinic forcing is expected to contribute to the development of these systems (Carrió et al., 2017; Fita et al., 2006). Cioni et al. (2016) highlighted that extra-tropical and tropical-like cyclone characteristics can alternate or even coexist in the same cyclonic system. In a recent study, Flaounas et al. (2021), who analyzed 10 medicane cases focusing on their mature phase, found that most of them develop under the influence of both baroclinic and diabatic processes. However, there are cases where a strong diabatic forcing plays the main role. In these cases, while a cyclone develops, increasing values of diabatically produced PV in its centre may eventually lead to tropical-like transition (Davis and Bosart, 2004). However, these seems to be rare cases, especially due to medicane's short lifespan compared to tropical cyclones, and to the frequent and sharp land–sea transitions that characterize the Mediterranean basin.

The advancements in satellite imagery, along with a comprehensive exploitation of all the available observations, have favored the clear identification and characterization of such peculiar events. In a recent study, Dafis et al. (2020) use infrared and microwave satellite diagnostics, in conjunction with model reanalysis, to study the evolution of deep convection in 9 medicanes between 2015 and 2018. They found that only a fraction of these cyclones experienced long-lasting intense convective activity close to their centers, and that the convection is deeper and more intense prior to the medicane maximum intensity, as also shown for some cases in previous studies (Claud et al., 2010; Marra et al., 2019; Miglietta et al., 2013). They also found that only deep convection in the upshear quadrants led to intensification, and that short-lived tropical-like structure develops only during symmetric convective activity.

With the advent of the Global Precipitation Measurement (GPM) mission era (Hou et al., 2014; Skofronick-Jackson et al., 2017), it has become possible to analyze the precipitation structure of medicanes as they form, develop and evolve up to their mature phase. The GPM mission consists of an international constellation of operational and research Low Earth Orbit (LEO) satellites carrying passive microwave (MW) radiometers, provided by a consortium of international partners, which are able to provide observations every 1.5 h (on average) over the Mediterranean area. The core of the constellation is the NASA/JAXA GPM Core Observatory (GPM-CO), which carries an advanced combined active/passive microwave sensor package, the GPM Microwave Imager (GMI), and the Dual-frequency Precipitation Radar (DPR). The DPR is the first spaceborne precipitation radar covering the Mediterranean area, even if its narrow swath (250 km compared to 850 km of GMI) makes its overpasses over specific events less frequent. The GPM-CO is currently considered the reference satellite-borne platform for the quantitative estimation of precipitation and for the precipitation microphysics characterization from space.

Panegrossi et al. (2016) illustrated the potential of the GPM constellation for monitoring heavy precipitation events over the Mediterranean area. They also showed the improved capabilities of the GMI with respect to other radiometers in depicting the rain band structure of medicane Qendresa, occurred on 7–8 November 2014 (no DPR overpasses were available for that case). In two later studies, Panegrossi et al. (2020) and Marra et al. (2019) illustrated GPM capabilities in monitoring the development and evolution of the storm Numa and of the associated surface precipitation, as it moved across the Ionian Sea, between 15 and 17 November 2017, and approached the south-eastern coast of Italy (Apulia region) where it persisted in its medicane phase for 24 h. The authors illustrated how the GPM-CO DPR measurements, available only during NUMA development phase, can be used, in combination with GMI, to identify medicane dynamical and microphysical processes. On the other hand, multiple GMI overpasses were used to identify specific features and their changes during the transition from the development to the mature stage, such as the stronger convective (and lightning) activity during the development phase, confirming what shown in earlier studies (e.g., Miglietta et al. (2013)). The authors also evidenced that during the medicane phase, strengthening or weakening periods in the eye development were observed, as well as the occurrence of warm rain processes in the areas surrounding the eye.

The more recent and very intense Medicane Ianos (Zalachoris, 2020), formed during mid-September 2020 over the Southern Mediterranean Sea. During its mature stage on 17–18 September, Ianos affected Southern Italy and especially Greece and its Ionian islands, where torrential rainfall and severe wind gusts caused widespread disruption, landslides, and casualties. Ianos has been identified as the most intense Medicane ever recorded by Lagouvardos et al. (2021), who reported a minimum sea level pressure of 984 hPa, wind gusts up to 54 ms^{-1} at its peak intensity when it made landfall in Greece, with record-breaking daily accumulated rainfall of 645 mm measured in the Ionian Island of Cephalonia. Four GPM-CO overpasses are available for Ianos throughout its evolution. For the GPM overpass on 17 September at 22:30 UTC, at Ianos peak of intensity and just a few hours prior to making landfall on the western coast of Greece, besides GMI, also DPR measurements are available capturing, for the first time, a medicane during its mature phase. Lagouvardos et al. (2021) analyze the genesis and evolution of Medicane Ianos using in situ observations available over the Ionian Islands, Meteosat Second Generation (MSG) SEVIRI imagery, combined with ZEUS lightning data, and model reanalysis. The authors also use three GPM-CO overpasses to analyze the precipitation structure during Ianos development and mature phase, pointing out the unique opportunity offered by the unprecedented DPR measurements. As opposed to other studies by Claud et al. (2010) and Miglietta et al. (2013), where deep convection was not detected close to the medicane center during its mature stage, the authors identified deep convection in proximity of the medicane core during Ianos mature phase, although no lightning activity was observed at that stage. Recently, the mature phase of Ianos has been examined by performing a sensitivity analysis of the Weather Research and Forecasting (WRF) model to different microphysics parameterization schemes and initial and boundary conditions (Comellas Prat et al., 2021). The authors use the GPM DPR measurements, and MetOp ASCAT sea surface winds, to verify WRF model forecast ability to reproduce the tropical-like features of Ianos during its mature phase as well as the 3D precipitation structure and its sensitivity to the different microphysics parameterization schemes. The authors also show that primary tropical-like features (low-level vortex, deep warm core, axi-symmetry, and surface winds) and the main rain band structure are well depicted by the model, although all microphysics

schemes tend to overestimate the intensity of the medicane and the convection strength compared to the DPR.

The goal of the present study is to analyze in detail the measurements of two of the GPM-CO overpasses available, one during Ianos development (16 September at 13:40 UTC) and one during its mature phase (17 September at 22:30 UTC), with the aim of carrying out a comparative analysis of the precipitation structure between the two phases. The strokes registered during the storm by the LINET network (Betz et al., 2004, 2007) are also used in the analysis as an additional verification tool. In particular, the combined GMI and DPR measurements, available during a medicane mature phase for the first time, are used to reconstruct the microphysical 3D structure as well as the intensity and nature of the convection in the outer rainbands and in proximity of the cyclone center, and to infer precipitation formation processes. In addition, the DPR measurements are used to verify what inferred from GMI measurements by taking advantage of their vertical sampling with respect to the integrated information derived from GMI. The GMI measurements available for both the overpasses are used to compare the microphysical and dynamical processes in the development and mature phase. The study aims at showing that: 1) different precipitation formation processes, as well as different strength and microphysical structure of the convection, can be inferred from the multi-sensor and multi-channel analysis of the GPM-CO overpasses in the development and in the mature stage; 2) these features can explain the change in the lightning activity observed during the two phases; 3) the GPM-CO provides, with unprecedented detail, evidence on the similarities of Medicane Ianos precipitation processes with tropical cyclones.

The paper is organized as follows: the Section 2 describes briefly the instrumentation and data used and provides general basic concepts of passive microwave multichannel analysis, the Section 3 reports the results which are discussed in the Section 4. Section 5 is dedicated to the conclusions.

2. Instrumentation and methods

2.1. GPM core observatory

The Low Earth Orbit (LEO) GPM Core Observatory (GPM-CO) is equipped with the two most advanced active and passive microwave sensors designed for precipitation retrieval from space: the Japan Aerospace Exploration Agency (JAXA) Dual-Frequency Precipitation Radar (DPR), and the National Aeronautics and Space Administration (NASA) GPM Microwave Imager (GMI) conically-scanning radiometer (Hou et al., 2014; Skofronick-Jackson et al., 2017). The DPR, a radar working at Ka- and Ku-band, allows to retrieve the horizontal and vertical structure of the precipitation and to characterize the particle size distribution thanks to the dual-frequency. The DPR measurements and products (Seto et al., 2013) are available for each of the three DPR scanning modes, i.e., the Normal Scan (NS) for Ku-band only, the Matched Scan (MS), combining Ka- and Ku-band measurements, and the High Sensitivity (HS) scan for Ka-band only. At the time of the present study, the NS DPR products were provided for the full swath (245 km width) for 49 footprints of 5 km diameter with a 125 m vertical resolution, while the MS DPR products were provided for the inner swath (120 km width) for 25 footprints at the same vertical resolution.[1] The DPR is also used as calibrator for all GPM precipitation products.

The GMI is a conical-scanning, total power MW radiometer equipped with 10 dual-polarization (V and H) window channels at 5 frequencies (10.65, 18.70, 36.5, 89.0 and 166.0 GHz) and three single-polarization (V) channels, one at 23.8 GHz and two in the water vapour absorption band at 183.31 GHz (V polarization). The GMI has 904 km wide swath, with a spatial resolution ranging roughly from 4 km × 7 km at the higher frequency channels (>89 GHz), 8 km × 14 km at 36.5 GHz, down to 19 km × 32 km at 10 GHz (see Draper et al. (2015) for further details). The central portion of the GMI swath overlaps the DPR swath. The GMI frequencies are currently considered as the most appropriate for detecting the wide spectrum of precipitation type and intensities, being the four high frequency channels at 166 GHz and 183.31 GHz particularly indicated for the detection of light precipitation and snowfall at higher latitudes (Hou et al., 2014; Panegrossi et al., 2017).

The combination of reflectivity measurements by the DPR and multichannels brightness temperatures measured by the GMI result in the combined DPR-GMI product (i.e. 2B-CMB) (Grecu et al., 2016), provided only for the MS and the NS. In this study, the 2B-CMB product V06A, providing corrected reflectivity profiles at Ku and Ka band, and different cloud and precipitation variables, is used along with GMI brightness temperatures (L1C product V05A) for the analysis of Medicane Ianos.

2.2. LINET network

The LINET network is a ground-based lightning detection system managed by nowcast GmbH, which is the owner of a significant number of measuring stations over Europe, covering also a large part of the Mediterranean Sea. Both cloud-to-ground (CG) and intra-cloud (IC) flashes can be detected by LINET sensor thanks to its working frequency range: in fact, the antenna is able to detect very low frequency and low frequency waves emitted during the flash. The detection of the lightning strokes is based on a pseudo-3D algorithm (Betz et al., 2007, 2004), described by the following three main steps:

- 2D location of the stroke through a time of arrival algorithm
- Exploitation of the time delay at the sensor nearest to the stroke
- Relaxation time of the travel path of the radio-wave

The capability of the pseudo-3D algorithm in estimating the height of the starting breakdown depends on the distance of the stroke from the antenna, which has to be lower than 100 km corresponding to the ideal situation where the distance between two LINET stations does not exceed 200 km, enabling both stations to detect the same event with the appropriate efficiency (Betz et al., 2007). The 2D location is possible thanks to the high-precision GPS clock equipped on each station. After locating the stroke, the algorithm considers the delay between the source of the lightning and the nearest station: the larger the delay, the more probable the stroke is an IC rather than a CG. Lastly, the relaxation time of the travel path is used to estimate the height of the discharge.

2.3. GMI imagery properties

The GMI imagery analysis of madicane Ianos is based on the use of the dual-polarization (V and H) 36.5, 89.0 and 166.0 GHz channels. The GMI lower frequency channels are not used in this study, since they are mostly used to infer surface rainfall intensity over the sea (as in Lagouvardos et al., 2021), and their lower spatial resolution does not allow to depict in detail the rainband structure. Moreover, these channels do not provide useful insights about the precipitation microphysics processes and convection strength. Table 1 shows synthetically a bulk interpretation of TB signals in the GMI frequencies considered in this study. For further details on the interpretation of MW TB imagery, refer to (Cecil and Zipser, 1999; Hourngir et al., 2021; Marra et al., 2017; Spencer et al., 1989) among many others.

In order to make the TB imagery independent from the surface emission properties, and to have a coherent precipitation-related signal regardless of the surface type (e.g., transition from land to sea), the

[1] The DPR operation mode described here refers to the situation prior to 21 May 2018. On that day, the DPR operation mode changed with the Ka-band radar matching the Ku-band radar over the full swath. However, the new DPR data structure, following the new DPR operation mode, has been made available only on December 6th, 2021, with the new release of the DPR algorithm.

Table 1
Synthetic interpretation of TB signals over sea surface at 37, 89 and 166 GHz.

GMI channel	TB Warmer than background	TB Colder than background
37 GHz	emission from raindrops (rain)	Scattering by large and dense ice (e.g. hail – deep convection)
89 GHz	emission from water vapour and cloud liquid water	Scattering by precipitating heavily rimed ice (e.g., graupel – convection/deep convection)
166 GHz	emission from water vapour and cloud liquid water	Scattering by less dense ice (snowflakes and aggregates – stratiform/convective precip)

Polarization Corrected Temperature (PCT) has been introduced in previous studies (e.g., Cecil and Chronis (2018)). PCT at 89 GHz and 37 GHz is used to analyze deep convection features at global and regional scale, as in (Hourngir et al., 2021) who carried out a climatological analysis of deep convection over the Mediterranean region. In this work, the PCT at a given frequency is defined following (Cecil and Chronis, 2018):

$$PCT_f = \left(1+\beta_f\right) \bullet TB_{fv} - \beta_f \bullet TB_{fh}$$

where β_f is a coefficient that minimizes the effects of surface emissivity and TB is the brightness temperature at frequency f and vertical (V) or horizontal (H) polarization. The PCT has the advantage of reducing the contamination due to the surface emissivity highlighting the cloud scattering signal. In this work, the PCT at 37 and 89 GHz has been analyzed using the coefficient $\beta_f = 1.15$ and $\beta_f = 0.70$, respectively, as reported in (Cecil and Chronis, 2018).

The polarization signal (i.e., the TB difference between the V and H polarization channels at a given frequency, hereafter ΔTB) can be exploited as a further diagnostic tool for precipitation characterization. The ΔTB at 166 GHz (note that GMI is the only MW radiometer with high-frequency dual-polarization channels) and 89 GHz provides a clear indication of the different type of solid-phase hydrometeors found in the cloud upper levels (Gong and Wu, 2017). At 166 GHz the high sea surface polarization signal (large ΔTB values) is not visible due to the water vapour absorption, therefore the presence of oriented ice hydrometeors in the upper cloud layers is evidenced by the increase of ΔTB with respect to the background. This occurs for example in the upper outflow region and in presence of stratiform precipitation. This effect is visible also at 89 GHz, while at this frequency the cloud liquid water has a strong depolarization effect on the surface background signal (low ΔTB values). At both frequencies a depolarization effect is also visible in presence of deep convective cores due to the tumbling heavily rimed or high-density ice particles (graupel or hail) sustained by the strong updraft (see also Marra et al. (2017)). At 37 GHz over sea, ΔTB can be used to identify areas of different precipitation intensity. High ΔTB values are found in correspondence of non-precipitating areas due to the highly polarized sea surface background. As the precipitation intensity increases, the ΔTB decreases due to the depolarization effect by the optically thick cloud.

Another useful tool used to interpret PMW imagery and characterize the precipitation microphysics properties is the analysis of GMI ΔTB-TB_v relationship for the high-frequency window channels (89 and 166 GHz) (see Gong and Wu (2017) for details). The characteristic bell-shape curve delineated by the ΔTB vs TB scatter plots (as shown in Fig. 9) is used here to analyze the different nature of the precipitation processes, and the strength of the convection, associated to Ianos, in the development and mature phase. For example, the presence and extension of the lower-left hand of the bell shape at 89 GHz (i.e., low TBs and ΔTBs associated due to strong scattering signal and depolarization effect) is a clear indication of the updraft strength, and of the presence of suspended heavily rimed, large ice particles.

3. Results

The depression that generated Medicane Ianos originated on the Libyan coast on 14 September 2020, then moved northward until it reached with its northernmost cloud bands the southern Italy coast, and finally bent towards Greece, where it made landfall at 03:00 on 18 September 2020. At that time, it reached the maximum intensity with 44 ms^{-1} sustained wind and 984.3 hPa minimum central pressure (Lagouvardos et al., 2021), equivalent to a Category 1 hurricane. Comellas Prat et al. (2021) report that Ianos reached its mature phase around 12:00 UTC on 17 September, and it lasted for about 18 h, until 06:00 UTC on 18 September. After landfall, Ianos lost most of its strength and moved southward to finally dissipate on 20 September 2020. Fig. 1 shows the trajectory of Ianos, described by the minimum mean sea level pressure (MSLP) obtained from ERA5 data (Hersbach et al., 2020), between 14 and 20 September 2020, with a sampling resolution of three hours. For each minimum MSLP point, the total number of strokes as detected by the LINET network within a time interval of ±30 min and within a 200 km radius from the position of the minimum MSLP are shown. The analysis evidences a significant lightning activity during the development stage (i.e. until about 12:00 UTC on 17 September 2020) followed by a sharp decrease of the activity, with almost no-lightning production within 200 km from the cyclone center during the mature stage. The lightning activity started again once Ianos' center hit the Greek coast (i.e. after 03:00 UTC on 18 September), even if with lower occurrence, until it disappeared at the final stages of the depression.

A more in depth analysis of lightning activity has been carried out for a period close to the mature stage of Ianos. Fig. 2 shows the number of total lightning (i.e. GC + IC) registered by LINET sensors every hour between 16 and 18 September at different distances from the position of the minimum MSLP. Most of the lightning activity occurred between 200 and 300 km from the position of the minimum MSLP with a peak of more than 8000 strokes per hour during the morning of 17 September. This confirms that the most intense convective activity occurs away from the cyclone center (Claud et al., 2010; Miglietta et al., 2013) with rates that are comparable to severe thunderstorms (e.g., Marra et al., 2017). A significant contribution to the total lightning is observed at a distance between 100 and 200 km from the minimum MSLP, with peaks above 1600 strokes per hour at 12:00 UTC on September 17. This is quite remarkable if compared to the lightning data recorded for other medicanes (Dafis et al., 2018; Marra et al., 2019; Miglietta et al., 2013). For example for Numa (Marra et al., 2019, Fig. 6) the hourly LINET stroke rates recorded within 200 km from the cyclone center are much lower (with a peak at 1100 strokes per hour) than those shown in Fig. 2 (orange curve). It is worth noticing that no LINET strokes are registered within 100 km from the center after 18:00 UTC on 16 September.

3.1. Analysis of GMI imagery

The GPM-CO overpassed Ianos four times during its lifetime (i.e. from 14 to 20 September 2020) allowing GMI wide swath to capture Ianos at each overpass, while DPR narrow swath (Ku-band NS) covers the storm only once on 17 September at 22:30 UTC. The DPR overpass provided, for the first time since the launch of the GPM-CO in 2014, 3D measurements of the precipitation structure and properties during a medicane mature phase. In this study, we focus on the analysis and the comparison of two overpasses, one at the development stage on 16 September at 13:40 UTC and one at the mature stage on 17 September at 22:30 UTC.

Figs. 3 and 4 show the maps of the TBs measured at 37, 89 and 166 GHz vertical polarization (V) channels (left column), and ΔTB for the same frequencies (right column), for the overpass on 16 September at 13:40 UTC and on 17 September at 22:30 UTC, respectively. Only one out the six panels (namely, panel c) shows also the strokes registered by LINET network within 15 min (i.e. ± 7.5 min) with respect to the time of

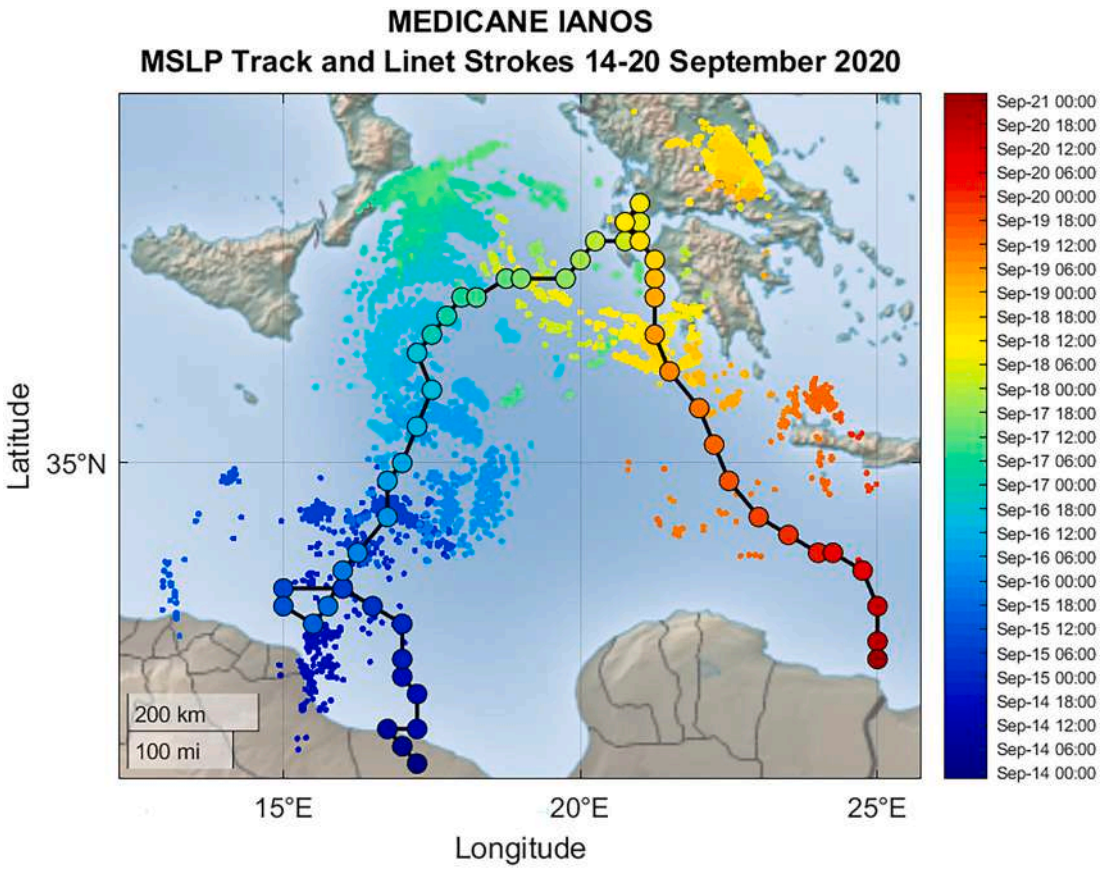

Fig. 1. Trajectory of Medicane Ianos as described by the position of the minimum MSLP value estimated by ERA5 data (dash-dot line). The smaller colored dots identify the position of strokes registered by LINET network within ±30 min and 200 km radius for each MSLP point.

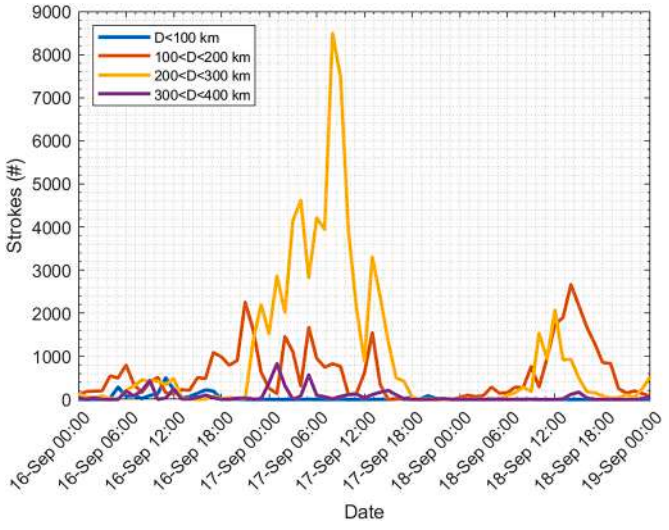

Fig. 2. Hourly trend of total lightning registered by LINET network from 16 to 18 September 2020 within different distances from the location of the minimum MSLP estimated by ERA5.

the GPM overpass, and within 400 km from the position of the minimum MSLP at the time closest to the GPM overpass. Fig. 3a, showing the 37 GHz TB imagery, evidences the presence of a wide area of precipitation (higher TBs with respect to the surrounding area) and the presence of scattering signal (colder TBs) in two areas of limited extension: one centered around 36.2°N, 16.6°E and the other one centered around 36.8°N, 17°E in the main rainband. The minimum TBs at 37 GHz reaching values between 215 and 230 K indicates the presence of deep convective cores and strong updraft, more intense with respect to medicane Numa, where the minimum TB values at 37 GHz were registered at 230 K in the development stage (Marra et al., 2019). The polarization signal (ΔTB) at 37 GHz (Fig. 3d) over sea clearly identifies areas of increasing precipitation intensity as ΔTB decreases (see Section 2.3).

Fig. 3b shows an extended area of low TBs ($< 230K$) at 89 GHz, with two regions of marked TB depression (minimum TBs at 135 K) in correspondence with the main convective cores, which appear larger and better defined than at 37 GHz due to the higher spatial resolution. The large comma-shaped low TB area at 89 GHz evidences the presence of suspended and heavily rimed ice particles in the upper-troposphere outflow region, around the main convective cores. These features are also visible at 166 GHz (Fig. 3c) (blue-cyan area), with TBs mostly between 165 K and 155 K, and around 140 K for the two main convective cores. At this frequency, an extended area of TB depression is visible (red areas with TBs around 240 K), due to the scattering by the complex-shaped and less dense ice particles (snowflakes or aggregates) present in the upper cloud layers of the outflow region. Fig. 3c also evidences the correspondence between the lightning location registered by the LINET network and the convective cores as identified by TB minima. The polarization signal (ΔTB) at 89 GHz (Fig. 3e) is governed mainly by the depolarization effect of the cloud liquid water. The blue-cyan region with ΔTB values below 6 K indicates optically thick clouds with large amounts of cloud liquid water associated to the precipitation (i.e., there is a close correspondence with the precipitation area identified by the ΔTB at 37 GHz). On the other hand, the green-yellow area (with ΔTB values between 10 and 20 K) indicates optically thinner clouds, with lower amounts of liquid water, in the non-precipitating portion of the storm. The ΔTB at 166 GHz (Fig. 3f) shows higher values (red-pink

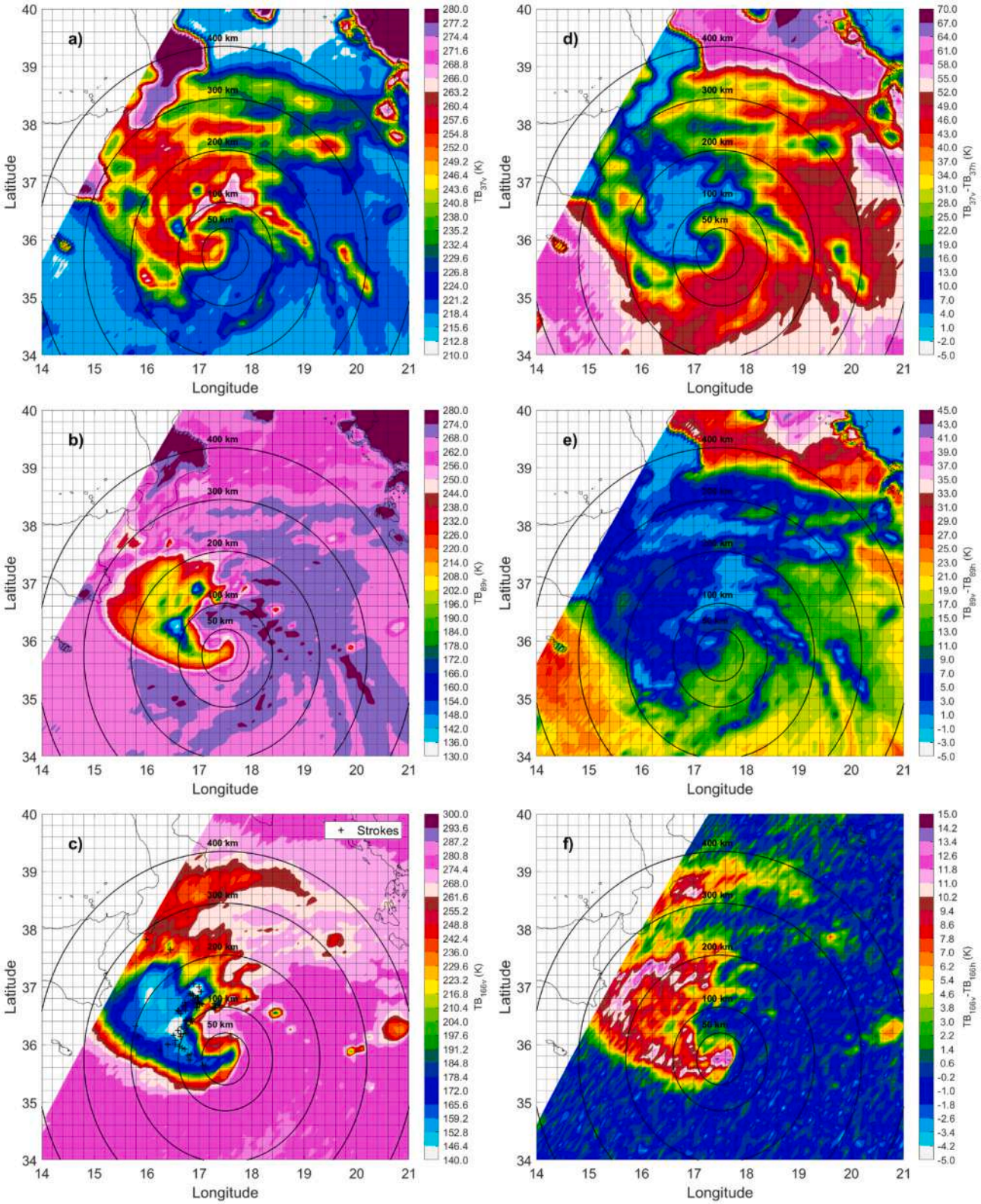

Fig. 3. Brightness temperature measured at a) 37 GHz, b) 89 GHz and c) 166 GHz v-pol channel by GMI radiometer for the overpass occurred in the development phase of Ianos on 16 September at 13:40 UTC. The difference between v-pol and h-pol channel brightness temperature measured at 37, 89 and 166 GHz are shown at panels d), e) and f), respectively. The black crosses (panel c) represent the lightning location as registered by LINET network within 15 min with respect to the GPM overpass.

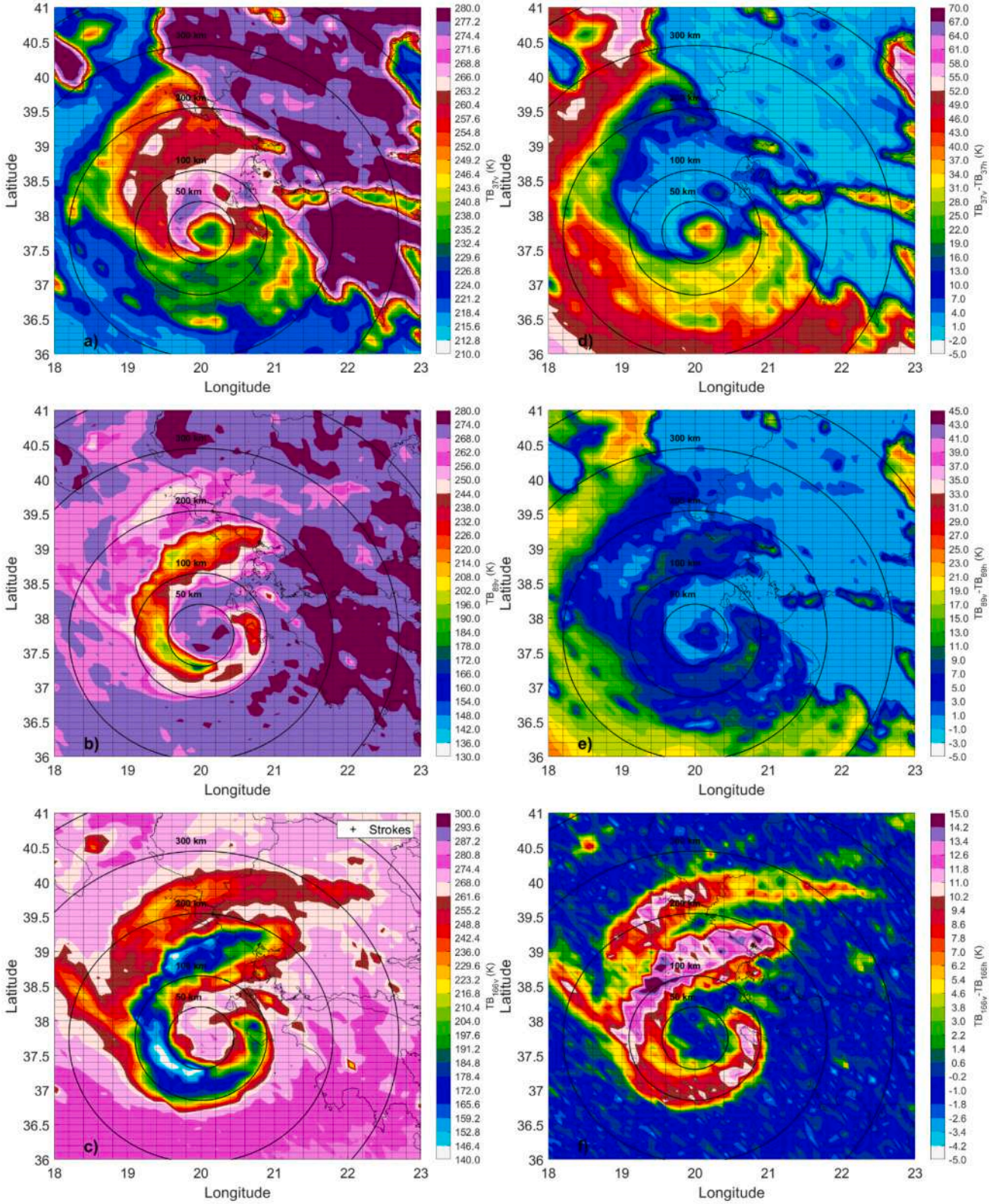

Fig. 4. Brightness temperature measured at a) 37 GHz, b) 89 GHz and c) 166 GHz v-pol channel by GMI radiometer for the overpass occurred in the mature phase of Ianos on 17 September at 22:30 UTC. The difference between v-pol and h-pol channel brightness temperature measured at 37, 89 and 166 GHz are shown at panels d), e) and f), respectively.

region with ΔTB above 7 K) associated with the upper outflow region or with stratiform precipitation, while the low ΔTB values (green areas, with ΔTB below 2 K) are found in correspondence with the most intense convective cores, and with the low-level clouds where the depolarization effect is due to the cloud liquid droplets.

The second GMI overpasses occurred on 17 September at 22:30 UTC capturing Ianos in its mature stage and it is shown in Fig. 4. The measurements show some similarities but also marked differences with respect to the previous overpass. Both overpasses evidence that most of the rain bands are located in the northern/north-western sectors of the storm. In Fig. 4a (TB at 37 GHz) a closed "eye", a roughly circular area within the 50 km radius of very light or no rain found at the center of the cyclone, one of the indications of the medicane mature phase, is well defined. The eye is surrounded by spiraling clouds, where convection is organized into long, narrow rainbands (which are oriented in the same direction as the horizontal wind, not shown). In the northern sector of the main rainband, the inner region within 100 km from the eye, shows higher TB values (pink-purple area with TBs above 262 K) than the outer region (red area with TBs below 260 K). In the southern sector, lower values of the TBs (green area with TBs below 240 K) are found. These transitions are related not only to the different intensity of the precipitation but also to the different precipitation microphysics processes during Ianos mature phase. The intensity of the precipitation can be inferred from the ΔTB map at 37 GHz in Fig. 4d. It evidences a region of very low or no precipitation in the southern sector and in the eye (ΔTB mostly above 30 K), while it shows more intense precipitation in the northern sector, with no significant changes in the transition between the two regions of the main rainband. From the analysis of the higher frequency channels, it is possible to distinguish the inner region of the main rainband characterized by shallow precipitation and warm rain processes, the presence of precipitation from mixed-phase clouds in the outer region, and non-precipitating clouds with high (frozen) cloud base. The warm rain precipitation is located north of the medicane eye roughly at the 50 km isoline. It is characterized by a significant warming at 37 GHz with respect to the background with TB values higher than 265 K (Fig. 4a), which does not correspond to TB depression at 89 or 166 GHz. For these channels, TB values higher than 255 and 260 K, respectively, highlight the absence of any type of ice particles. The low ΔTB values close to 0 K at 37 GHz and 89 GHz around the eye are an additional confirmation that those are heavy rain pixels associated to large amount of cloud liquid water. On the other hand, the non-precipitating clouds in the southern sector, roughly between 50 and 100 km isolines, identified by the 37 GHz channel analysis (Fig. 4a, d), are characterized by TB depression at higher frequencies, more marked at 166 than 89 GHz (Fig. 4b-c), due to the scattering by the ice in the upper levels, evidenced also by the high ΔTB values at 166 GHz (Fig. 4f), ranging between 10 and 12 K indicating the presence of oriented ice particles.

The presence of precipitation from mixed-phase clouds is evident in the rainbands around Ianos eye. TB depression at both 89 and 166 GHz channels (Figs. 4b-c) is observed in the inner rainband, while TB depression only at 166 GHz is observed in the outer spiral rainbands. It has to be highlighted that the TB depression at 89 GHz in the mature stage, reaching values down to 175 K, is weaker than what observed at Ianos development stage (Fig. 3b). At the same time, there is no scattering signature at 37 GHz (as opposed to the development phase shown in Fig. 3a), indicating the absence of very strong updraft. This suggests that: 1) the inner rainband exhibits convection features but, as opposed to the development phase, it seems to be characterized by weaker updraft, with formation of rimed ice particles (graupel) of limited size able to scatter the radiation at 89 GHz (and 166 GHz), but not at 37 GHz; 2) most of the outer spiral rainbands can be associated to stratiform rain, as evidenced by the scattering signal at 166 GHz due to the (oriented) ice hydrometeors in the upper levels. This is also confirmed by the analysis of ΔTB both at 89 and 166 GHz (Fig. 4e-f) which shows positive values up to 15 K, evidencing the presence of stratiform precipitation (Gong and Wu, 2017). Further evidence of the different nature of the convection (and lack of strong updrafts) at this stage compared to the development phase, is provided by the LINET network which did not record any strokes in the time and space interval around the GPM-CO overpass (see also Fig. 2).

3.2. Analysis of DPR overpass during Ianos mature stage

Useful insights on Ianos precipitation structure and characteristics during its mature phase are provided by the DPR measurements available for the GPM-CO overpass on 17 September at 22:30 UTC. DPR is also used to verify the interpretation of GMI measurements described in Section 3.1. Fig. 5 reports the corrected reflectivity at Ku-band (Z_{Ku}) at near surface level (the first level from the surface not affected by ground clutter), the storm top height (STH), as well as the maximum Ku-band corrected reflectivity value ($MaxZ_{Ku}$) found along the vertical profile of each DPR footprint, and the height of the maximum Ku-band corrected reflectivity value (H-$MaxZ_{Ku}$). What is immediately clear is that the rainband structure is coupled mostly to moderate precipitation intensity as highlighted by the Z_{Ku} values (Fig. 5a). Most of the DPR footprints show Z_{Ku} values lower than 38 dBZ, while only a limited number (namely the 6.5%) of footprints slightly exceed 40 dBZ. The $MaxZ_{Ku}$ (Fig. 5c) confirms the situation depicted near the surface. It does not exceed 45 dBZ, with the most intense areas found around the radar scan line (DPR cross-track direction) 94 and between rays (DPR along-track direction) 37 and 45 shown in the figure. At the same time, the STH variable shows the vertical extension of Ianos rainbands not exceeding 11 km (Fig. 5b). It is worth noting that, due to the well-known sensitivity limitation of DPR, generally, the STH does not coincide with the cloud top height, except for some particular cases (e.g. for the anvil the cloud top is identical to the STH) (Iguchi et al., 2018b). The analysis of the H-$MaxZ_{Ku}$ evidences that, for most of the DPR footprints, the level of the most intense precipitation does not exceed the height of the freezing level, which ranges between 4 km and 5 km (see Figs. 6 and 7). This demonstrates that almost the totality of the precipitation can be classified as stratiform precipitation. Only a small cluster close to the south/south-west portion of the inner rainband of Ianos shows convective properties with high values of both STH and H-$MaxZ_{Ku}$; this is also confirmed by the analysis of precipitation type variable provided by DPR (not shown). Fig. 5 confirms two other interesting features inferred from the GMI TB imagery analysis (Section 3.1), namely, the non-precipitating clouds in the southern sector and the warm rain area in the northern sector surrounding the eye. The non-precipitating clouds can be roughly located south of 37.4°N by observing that: 1) Z_{Ku} at near surface level is below the minimum detectable signal of DPR (Fig. 5a); this can be associated to the absence of (or very low intensity) precipitation; 2) the STH values are among the highest (up to 11 km) in the study area, indicating high level clouds (Fig. 5b); 3) the maximum Z_{Ku} values are quite low, between 20 and 25 dBZ, denoting the presence of small, probably frozen, particles (Fig. 5c); 4) the height of maximum Z_{Ku} is above 6 km indicating the presence of high cloud base (Fig. 5d). The warm rain region can be located in the 19.5–20.5°E, 37.9–38.6°N area by observing that: i) the STH is mostly lower than 4 km except for some small cluster where it reaches values as high as 5 km (Fig. 5b); ii) the difference between the Z_{Ku} at near surface level and the $MaxZ_{Ku}$ is generally close to zero (not shown) highlighting as the coalescence is the most effective precipitation formation process (Fig. 5a and c) (D'Adderio et al., 2018); iii) H-$MaxZ_{Ku}$ is the lowest in the study area confirming the analysis at the point ii) (Fig. 5d).

The analysis of the vertical cross sections of DPR measurements offers further details of Ianos structure and processes inferred from the GMI TB analysis. The cross-sections are shown across Ianos eye for ray 37 (along track) and scan line 122 (cross-track), in Fig. 6, and across a convective and stratiform region (see Fig. 5) for ray 45 and scan line 94 in Fig. 7. The top row of Fig. 6 shows the vertical cross section (ray 37) in the North-West/South-East direction. Moving from North to South and

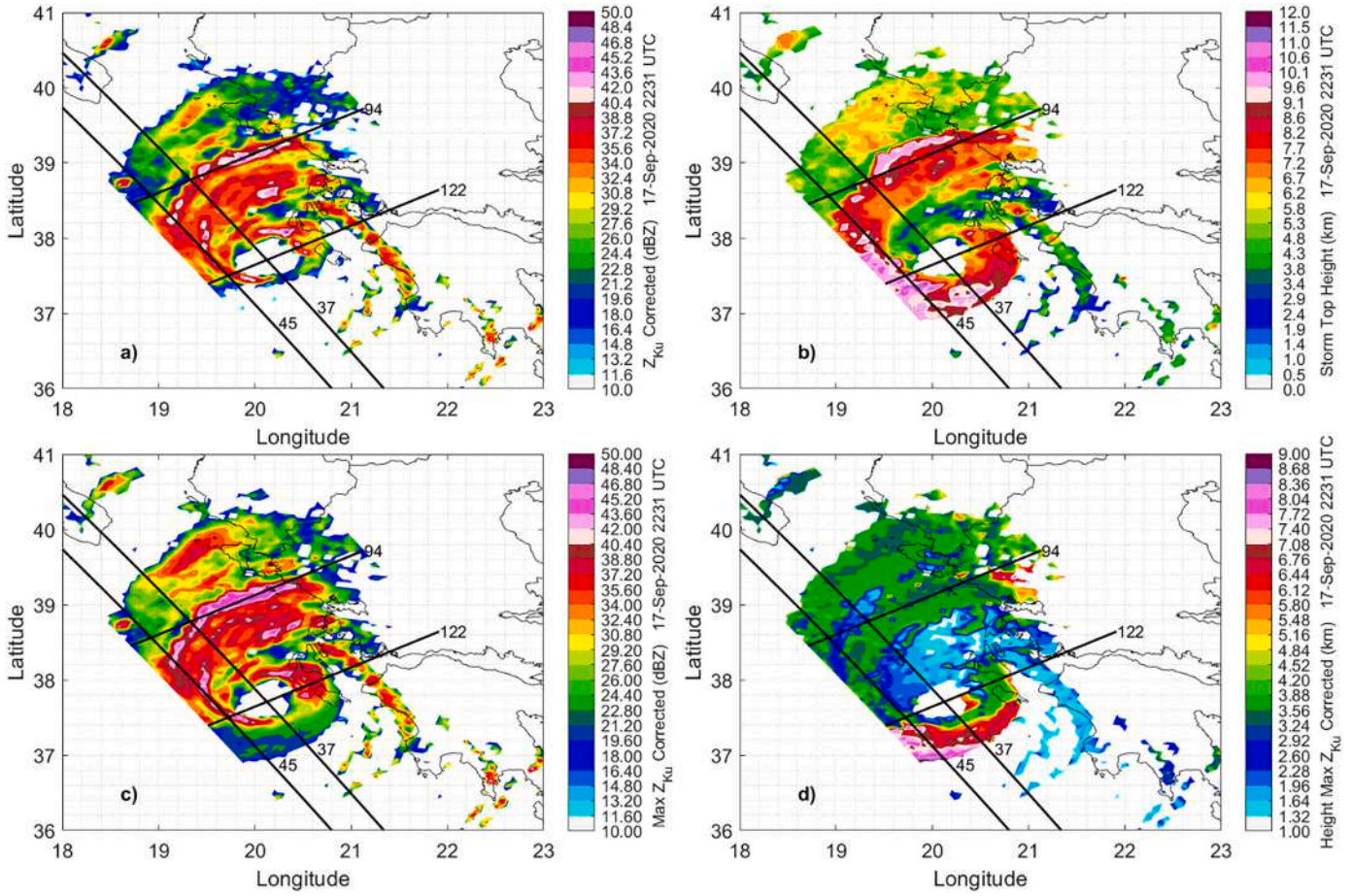

Fig. 5. a) Ku-band corrected reflectivity at Near Surface level; b) storm top height, c) maximum Ku-band corrected reflectivity and d) height of the maximum Ku-band corrected reflectivity. Ku-band radar scan lines 94 and 122 and rays 37 and 45 used for the vertical cross-sections in Fig. 6 and Fig. 7 are also shown as black lines.

looking at the Z_{Ku} (Fig. 6a), five different zones can be identified by dashed-dot vertical lines. A first stratiform zone (zone I) between 18.8°E and 19.3°E with a clear bright band; in the 19.3°E-19.8°E range there is another region (zone II) with deeper clouds showing (moderate) embedded convection features (40 dBZ echo top eight around 4 km), and STH reaching 8.5 km height in the outer region, and decreasing towards the cyclone center down to 4 km. Then, in the 19.8°E-20°E range, the warm rain region (zone III) can be identified, with Z_{Ku} exceeding the minimum detectable signal at height around 4 km. Ianos eye (zone IV), located between 37.8°N and 37.45°N (20°E-20.3°E), is followed by a quite weak and narrow rainband and by a non-precipitating high-level cloud, with cloud base ranging between 4.5 and 6 Km (zone V). The rainfall rate values at the lowest available bins (not shown) are generally lower than 10 mmh^{-1} with only some bins slightly exceeding 20 mmh^{-1}. The mean mass-weighted diameter (D_m) shows values generally lower than 1.5 mm (Fig. 6b), with only the northern part with embedded convection reaching values as high as 2 mm. The scan line 122 (Fig. 6, bottom row) presents three different precipitation structures. Moving from East to West, we first see the inner rainband (zone I) characterized by deep convection (evidenced in Fig. 4b by the low TBs at 89 GHz) with Z_{Ku} values up to 45 dBZ at 5 km, and the storm top reaching 11 Km (Fig. 6c) (with high rainfall rate values, exceeding 50 mmh^{-1} along the vertical profile, not shown), followed by the Ianos eye located between 19.8°E and 20.25°E (zone II). This is followed by shallower, mostly stratiform clouds (with embedded convection) evidenced by the bright band (zone III). It is worth noting that the bright band appears slanted due to the increasing freezing level height (black solid line) towards the medicane center. This is a clear indication of the warm core anomaly characterizing the medicane mature phase. The outer, narrow rainband centered around 21°E, which corresponds to the rainband approaching the Peloponnese coast in Fig. 5, exhibits shallow precipitation features with storm top not exceeding 6 km (zone IV). This explains the lack of scattering signature at 89 and 166 GHz in Fig. 4b/c, while the fact that this rainband is hardly visible at 37 GHz is due to the contamination of the emission signal by the land surface. The D_m values are generally lower than 1.5 mm (Fig. 6d), except for the eastern part of the convective region (zone I) showing a peak of D_m (2–2.5 mm) between 4 and 6 km, highlighting that the collisional break-up is the dominant precipitation formation process (D'Adderio et al., 2018).

Looking at Fig. 7, the vertical structures depicted by ray 45 and scan line 94 are quite different from each other. Moving from North to South on the ray 45, three different regions can be identified (Fig. 7, top row). A first, very weak and shallow precipitation region (zone I), between 18.6°E and 19.1°E, with D_m generally lower than 1 mm (Fig. 7b). A second region (zone II), more extended, between 19.1°E and 19.8°E characterized by convective precipitation, becoming deeper and more intense around 19.5°E, with high Z_{Ku} values exceeding 45 dBZ (Fig. 7a) (and rainfall rate exceeding 10 mmh^{-1} or even 30 mmh^{-1} along the most intense profiles, not shown), a significant vertical extension reaching 9 and 11 km and where D_m shows similar properties to the convective region along scan line 122 (Fig. 7b). A final non-precipitating, high-level cloud region (zone III) is visible further to the South-east, showing very similar properties with respect to the corresponding region along ray 37 (Fig. 5, top row). This analysis confirms what has been evidenced through the analysis of multichannel GMI TBs in Fig. 4. In particular, the DPR provides evidence of the convective

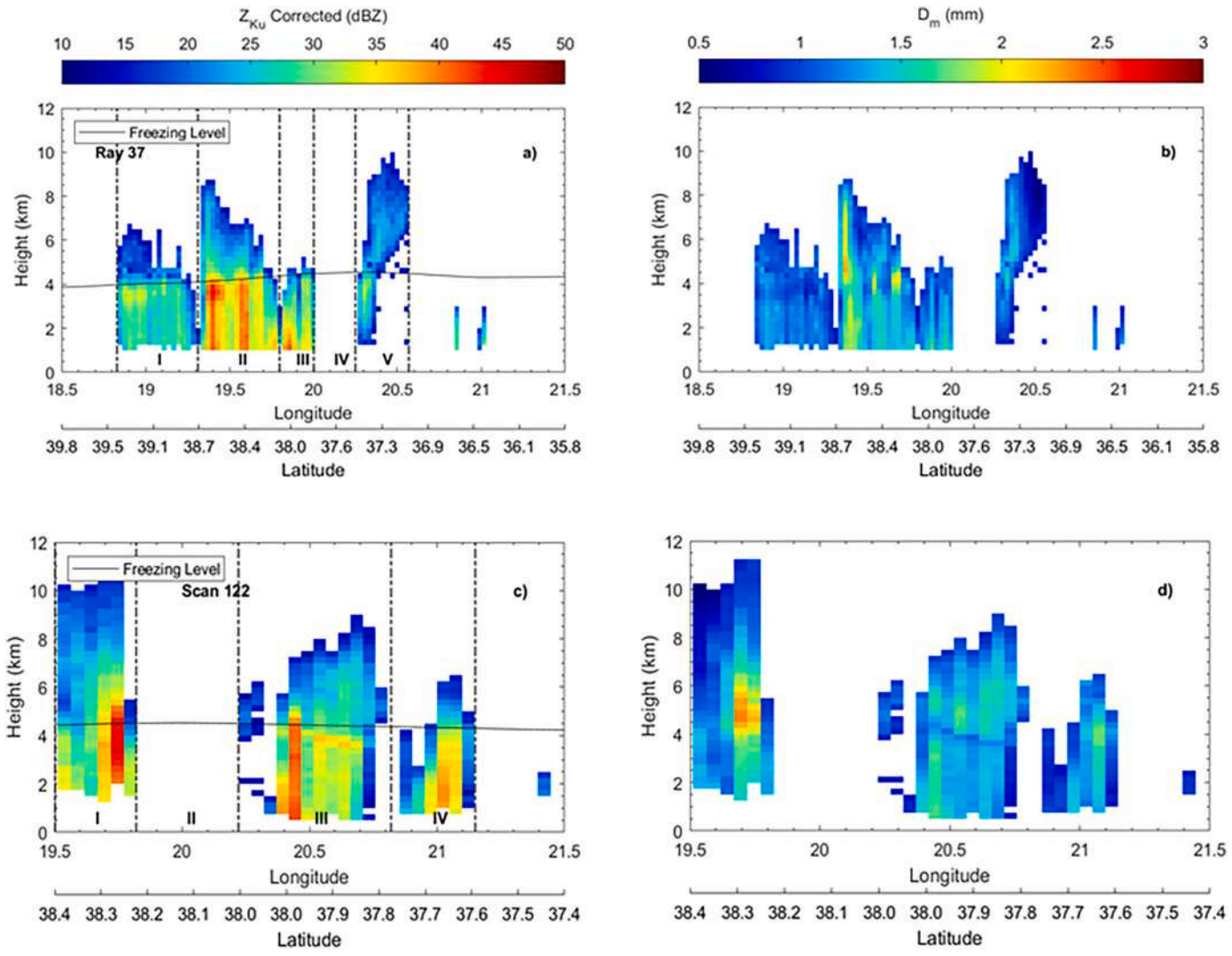

Fig. 6. Vertical cross-section of Ku-band corrected reflectivity (panels a / c) and mean mass-weighted diameter (panels b / d) for ray line 37 (top row) and scan line 122 (bottom row).

nature of the inner rainband, more intense in the region between 19.5°E and 20°E where the minimum TBs at 89 GHz are observed, associated to heavy precipitation. The characteristics depicted by scan line 94 (Fig. 7, bottom row) are typical of stratiform precipitation (zone II), with a marked bright band around 3.8 km (the freezing level is constant along the whole scan line at 4 km), where the reflectivity reaches values close or even higher than 40 dBZ along the whole scan line (Fig. 7c). The vertical extension of this rainfall region is significant, mainly between 7 and 9 km (such situation reflects in rain rate values generally between 7 and 20 mmh^{-1}, with peak values at 30 mmh^{-1}, not shown). The D_m shows increasing values moving from the bright band towards the ground (Fig. 7d) highlighting that coalescence is the most effective microphysical process for stratiform precipitation (D'Adderio et al., 2018). This also confirms what was outlined in the GMI multichannel TB description about the stratiform cloud features in the outer rainband, characterized by significant scattering signature and significant polarization signal at 166 GHz. This wide stratiform region is preceded by a weak shallow precipitation region (zone I).

3.3. Analysis of Ianos convection and precipitation processes

The analysis of the PCT, calculated for the 37 and 89 GHz channels both for the development and for the mature stage of Ianos and shown in Fig. 8, allows to identify a TB depression exclusively related to the scattering by the ice hydrometeors affecting these frequencies, therefore indicating the presence and intensity of convection. During the development stage (top row), two cores with significant PCT depression are evident at both 37 and 89 GHz (Fig. 8a-b). PCT values as low as 220 and 130 K, respectively, corresponds to the deep convective cores highlighted in the analysis of Fig. 4. In particular, the minimum PCT values at 37 GHz can be associated to the presence of large amounts of high-density, large ice hydrometeors (i.e., graupel, hail) whose growth is favored by the strong updraft. On the other hand, the PCT calculated at the mature stage (bottom row) of Ianos evidences different convection features with respect to the development stage. The weak PCT depression at 37 GHz, with the lowest values around 250 K (Fig. 8c) and the more marked PCT depression at 89 GHz, with values approaching 180 K (Fig. 8d), correspond to the third intensity class (accounting for 1% lowest PCT values) of the deep convection feature classification provided by Hourngir et al. (2021). However, the PCT depression is much less pronounced than during the development phase, where the PCT values at 89 GHz falls in the second intensity class (0.1% lowest PCT values) of the Hourngir et al. (2021) deep convection feature classification. This indicates the presence of weaker updraft and rimed ice particles (graupel) smaller in size then during the development phase, probably drifted away by the strong horizontal wind in a slanted

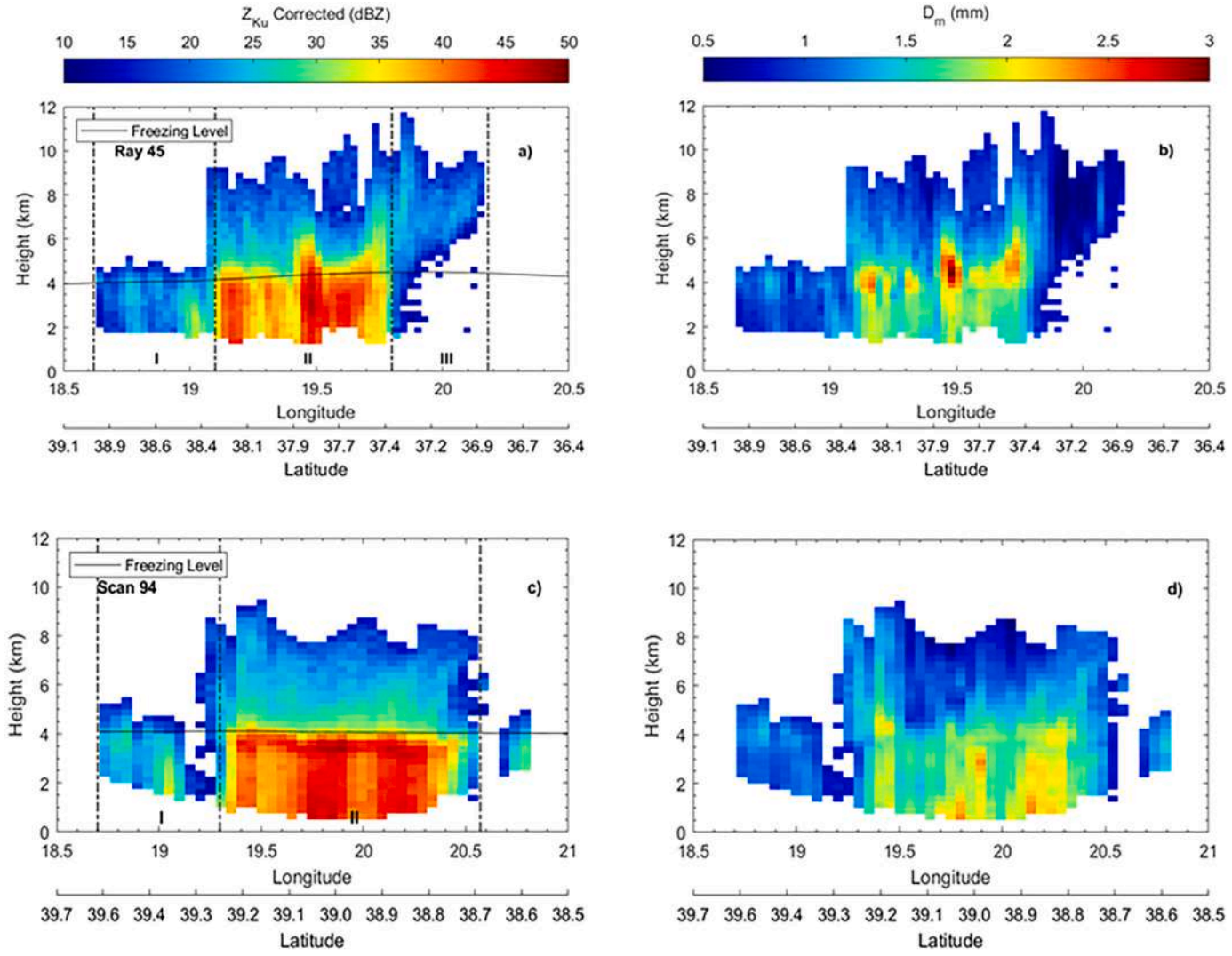

Fig. 7. Vertical cross-section of Ku-band corrected reflectivity (panels a / c) and mean mass-weighted diameter (panels b / d) for ray line 45 (top row) and scan line 94 (bottom row).

trajectories in the inner rainband, limiting the possibility of electrification processes and lightning activity, as it will be discussed in Section 4.

Fig. 9 reports the ΔTB-TB_v relationship at 89 and 166 GHz, respectively, only for GMI footprints over sea. The selected footprints have been labeled with different colors to indicate four different precipitation processes/characteristics, delineated according to different thresholds on the TB, the ΔTB, or the PCT, defined empirically from the analysis of Figs. 4, 5, and 8, or from the literature (Table 2).

The threshold set on PCT at 89 GHz to identify deep convection (black dots) is based on the study by Hourngir et al. (2021), corresponding to the upper limit for the 0.9% class of coldest values found for a 4-year analysis over the Mediterranean, and confirms that a large number of deep convection pixels are found during the development stage of Ianos. The $\Delta TB_{37GHz} < 30$ K threshold, based on the analysis of Fig. 4d, corresponds to 83.2% (1.9%) of the DPR rain (no-rain) footprints. It is worth noting that the different conditions can be verified simultaneously. For instance, a deep convection pixel (black dot) presents ice on top (green dot) and it is also a rainy pixel (blue dot). Moreover, footprints where at least one LINET stroke occurred within ±7.5 min with respect to the GPM overpass are also highlighted by red-circles. The circle size is an indication of the number of the LINET strokes occurred within the footprint. The ΔTB-TB_v relationship at both development (Fig. 9a-b) and mature (Fig. 9c-d) stage of Ianos shows the typical bell shape (see Gong and Wu, 2017) better depicted at 166 GHz than 89 GHz, and well defined during the development stage. The ΔTB peaks around 10 K for TB around 220 K and 190 K at 89 and 166 GHz, respectively, is in perfect agreement with what found by (Gong and Wu, 2017). Most of the selected pixels are rainfall pixels (ΔTB_{37GHz} <30K). The low ΔTB values (close to zero) at the left and right hand of the bell curve correspond, respectively, to deep convection (see Section 2.3) and shallow precipitation (high TBs due to the low scattering signal, and low polarization signal due to the precipitation and cloud liquid water). It is worth noting that the behavior of the bell curves are not related to surface precipitation intensity but mostly to the precipitation formation processes. Pixels with larger values of ΔTB fall in the "ice on top" class (green dots), and correspond either to stratiform precipitation with a well defined deep ice layer above the freezing level, or to no-rain pixels (green-only dots) (more numerous during the mature than the development stage) are. A small cluster of warm rain pixels (magenta dots), characterized by large TB values at 89 GHz and at 166 GHz, is present in the lower-right hand side of the bell curves. The striking difference in the left-hand of the bell curve between the development stage (Fig. 9a-b), characterized by lower TB values at both 89 and 166 GHz and by the presence of LINET strokes, and the mature stage (Fig. 9c-d), is an immediate indication of the different nature and intensity of the convection between the two phases.

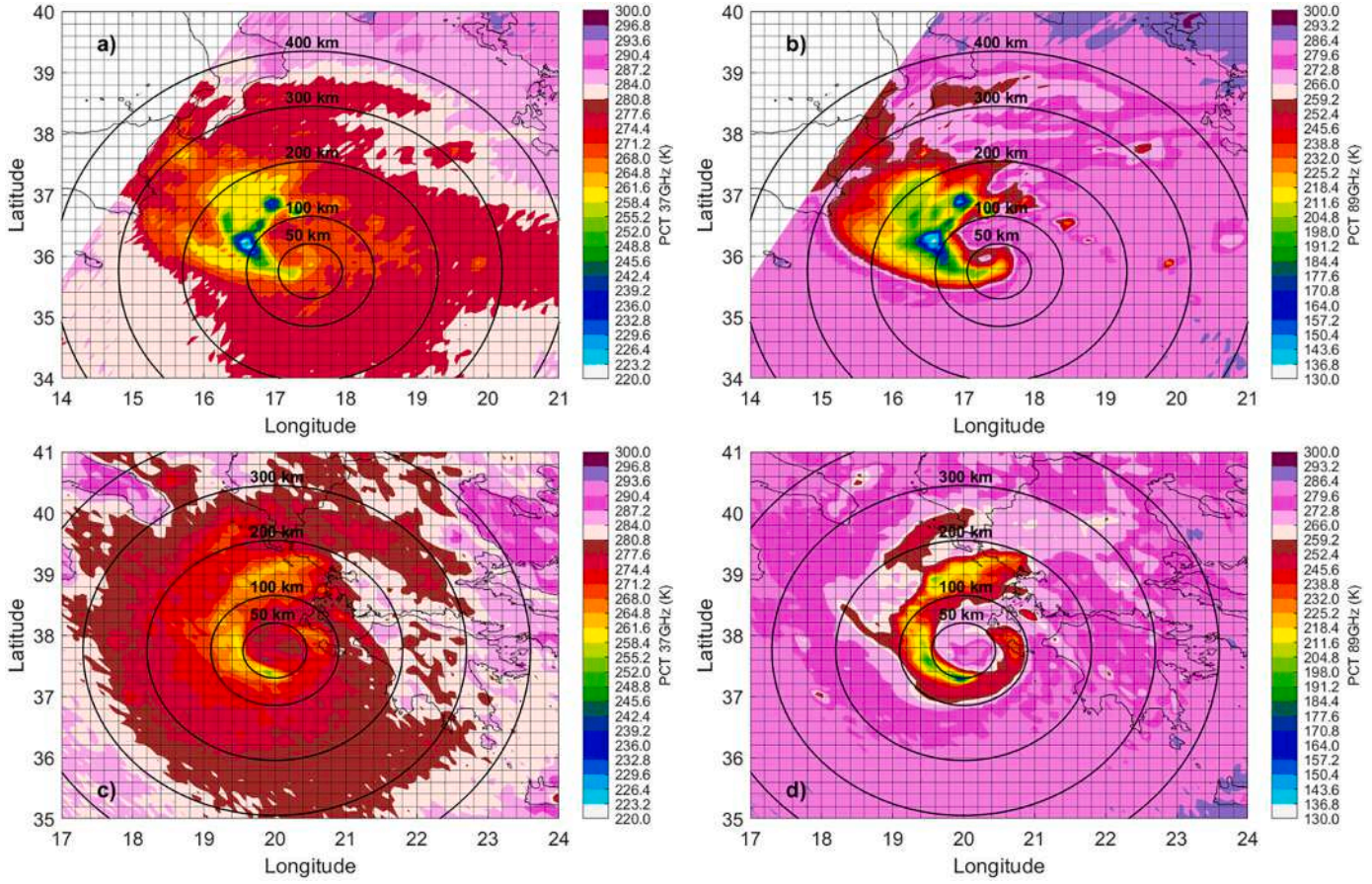

Fig. 8. PCT computed at 37 (left column) and 89 GHz (right column) for the development (top row) and the mature stage (bottom row) of Ianos.

A sort of validation of the precipitation structure classification reported in Fig. 9, inferred from GMI measurements only, can be provided for Ianos mature stage by the DPR measurements for the pixels where passive and active microwave information can be combined. To this end, the distribution of the difference between the freezing level (FL) and the storm top height (STH) as provided by DPR for the different precipitation classes defined in Fig. 9, is shown in Fig. 10. Both deep convection (black line) and warm rain (magenta line) classes show a quite narrow distribution peaking around −6 km and 0 km, respectively. This evidences the reliability of the GMI-based classification, with negative FL-STH values indicating the deep vertical extent of the clouds, and positive (or close to zero) FL-STH values indicating that the precipitating cloud top is close to (or below) the FL. It has to be highlighted that the FL provided by DPR is obtained from ancillary data (i.e. the JMA Global Analysis (GANAL) product) and some deviations from its real values, especially for small scale features such as the limited-size warm core, may occur (as evidenced in the discussion of Fig. 6d). The FL-STH distribution for the "ice on top" class shows only negative values with the highest occurrence between −3 and − 6 km. The FL-STH distribution of the rain class is the widest being comprehensive of all the other classes.

The analysis of Figs. 9 and 10 reveals as the mature stage of Ianos is characterized by very limited convective activity and by a cluster of non-precipitating high-base clouds. This GMI-based analysis is further verified using the DPR product variables. In particular, in Fig. 11 the deep convection class pixels are superimposed to the map of the maximum height at $Z_{ku} \geq 20$ dBZ (Fig. 11a), while the no-rain "ice on top" class pixels are overlapped to the precipitation rate at near surface level (Fig. 11b). The maximum height at $Z_{ku} \geq 20$ dBZ shows the limited vertical extension of Ianos with values generally lower than 7.5 km. Higher values, roughly between 9 and 10 km, can be found in correspondence with the deep convection pixels (Fig. 11a), highlighting the excellent agreement between the 89 GHz PCT-based classification and the precipitation vertical structure observed by DPR. In the same way, the "ice on top" non-precipitating pixels are located in the region where the DPR rain rate map shows null values (Fig. 11b).

4. Discussion

Two GPM-CO, overpasses available during Ianos intensification phase are analyzed in this study: one on 16 September at 13:40 UTC capturing Ianos at its development phase and one on 17 September at 22:31 UTC at its mature phase. The LINET strokes registered during the storm evolution are used to monitor the lightning activity associated to it and as further verification tool in the GPM-based analysis of deep convection processes during the two phases.

The analysis of LINET data evidences how the mature stage of Ianos was characterized by a total absence of lightning activity within 400 km radius from the minimum MSLP (corresponding to the medicane eye during Ianos mature phase). On the other hand, the maximum flash rate was recorded between 20 and 24 h before the Ianos maximum strength reached at 03:00 UTC on 18 September 2020 (Comellas Prat et al., 2021). This is in agreement with the temporal range found in other studies which analyzed both tropical cyclones and Mediterranean TLCs (Dafis et al., 2018; Miglietta et al., 2013; Zhang et al., 2012). However, a second and slightly more isolated flash rate peak was recorded roughly 12 h before Ianos maximum intensity showing similar characteristic to medicane Numa (Marra et al., 2019). Another similarity with medicane Numa was the contribution to the total lightning that comes mainly from the rain bands far away from the medicane center (i.e. for distances between 200 and 300 km). On the other hand, the hourly flash rate intensity (i.e. the number of total flashes per hour) was markedly higher than the values registered for other medicanes, with a peak reaching

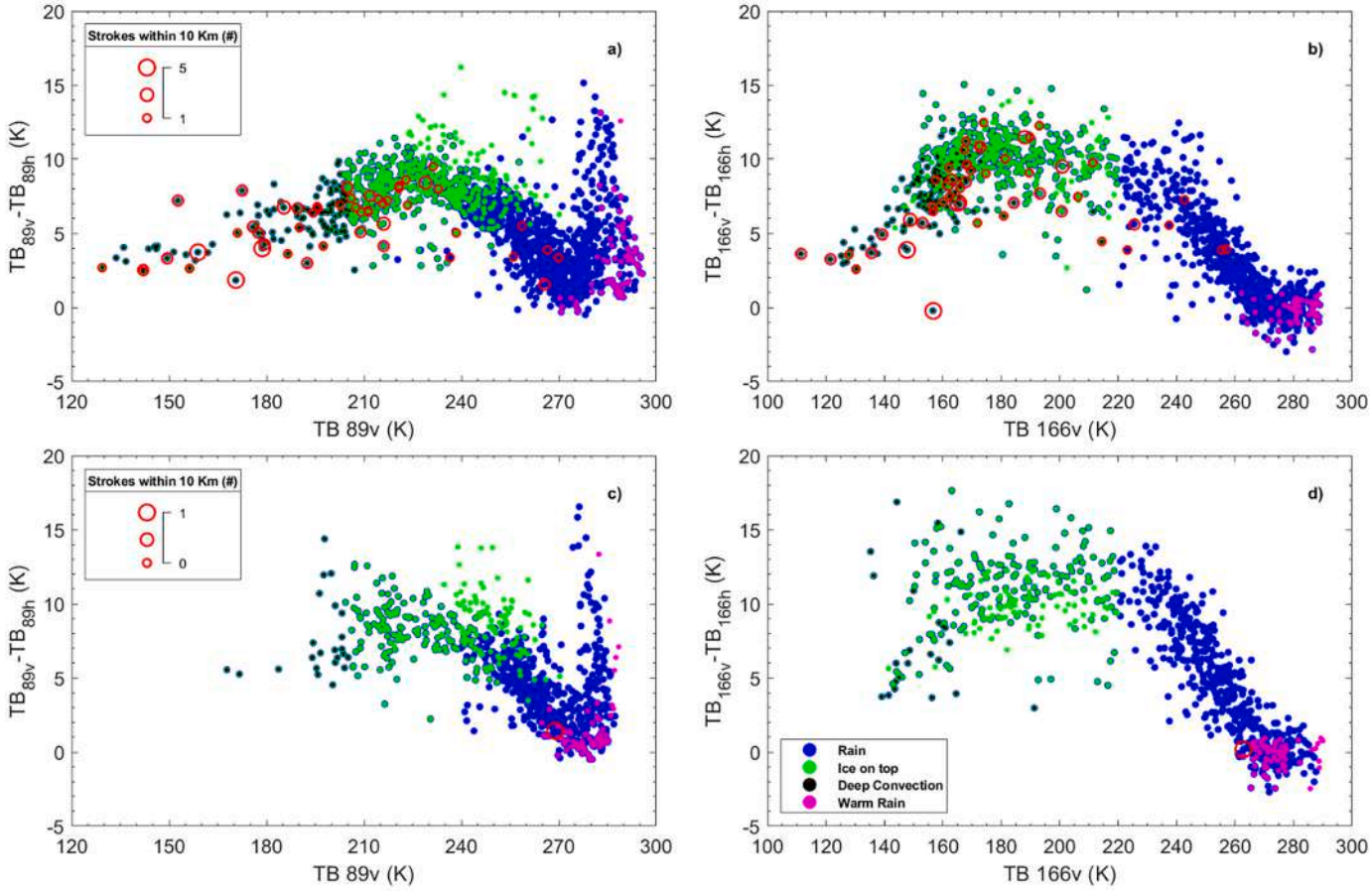

Fig. 9. ΔTB vs TB at 89 (left column) and 166 GHz (right column) for the development (top row) and the mature stage (bottom row) of Ianos for pixels over sea. The dots color corresponds to the different conditions set on ΔTB, TB or PCT **as defined in** Table 2.

Table 2
four precipitation classes identified by different thresholds on the TB, the ΔTB, or the PCT.

Precipitation class	Threshold
Rain	$\Delta TB_{37GHz} < 30$ K
Ice on Top	$TB_{166GHz} < 220$ K
Deep Convection	$PCT_{89GHz} < 210$ K
Warm Rain	$TB_{37GHz} < 268$ K & $TB_{166GHz} > 261$ K

9500 flashes per hours. The lack of lightning activity during Ianos most intense phase has been reported by (Lagouvardos et al., 2021), and is a typical feature of the medicane's mature phase observed in several other studies (e.g., Marra et al., 2019; Miglietta et al., 2013), indicating that high horizontal wind speeds at medicanes' mature stage inhibit electrical activity. There is actually a time lag between electrical activity and maximum intensity, a behavior that has been reported also for tropical cyclones (Cecil and Zipser, 1999). Electrical activity is more likely in regions with substantial updraft, where mixed-phase regions occur with graupel, supercooled cloud water, and vapour-grown ice crystals in the charging zone, i.e. between −15° and −25 °C (Formenton et al., 2013), and results first from gravitational separation of particles carrying different signs of charge, followed by differential advection of net charge regions (Willis et al., 1994). Such conditions are evidently satisfied during Ianos development phase and not during its mature phase. As observed by Black and Hallett (1999) in their study on electrification processes in hurricanes, even if charge separation occurred in multiple locations in the eyewall or in the rainbands, the strong horizontal winds ensure that charged particles become widely dispersed in a relatively short time, thereby weakening both the horizontal and vertical gradients of charge, resulting in lower probability for the cloud electrification and for chances of lightning. A similar mechanism is likely responsible for the lack of electrical activity observed during Ianos (and most medicanes) mature phases.

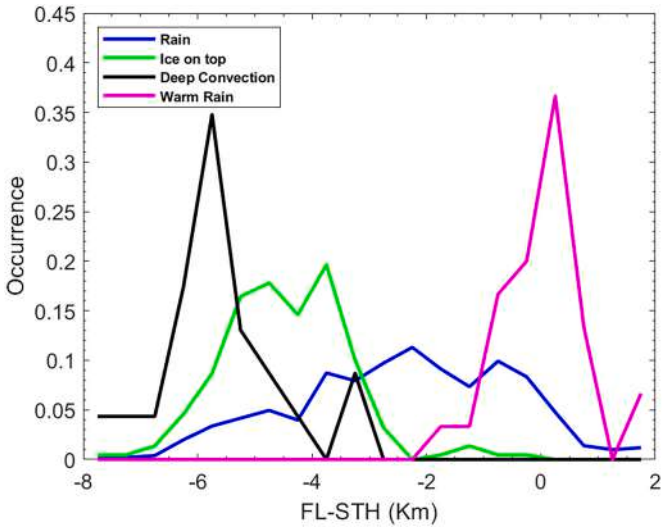

Fig. 10. distribution of the difference between the freezing level (FL) and the storm top height (STH) as retrieved by DPR for the mature stage of Ianos. The same thresholds used in Fig. 9 are used to selected the pixels.

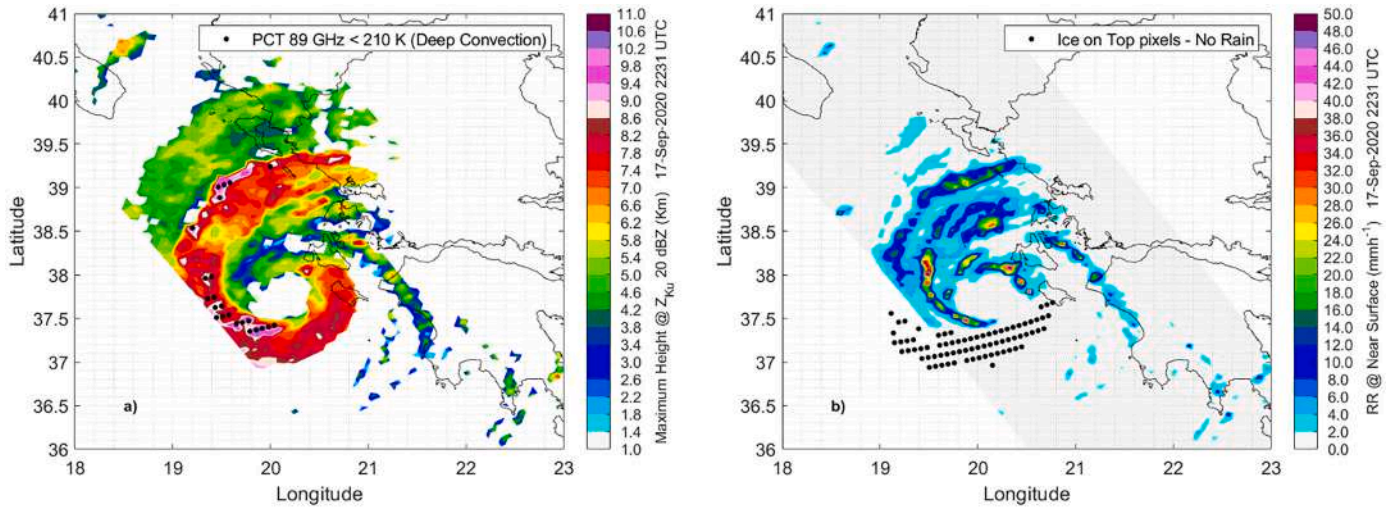

Fig. 11. a) map of maximum height for $Z_{ku} \geq 20$ dBZ overlapped by the deep convection class pixels and b) map of the rain rate at near surface level overlapped by ice on top not precipitating class pixels.

The nature of the convection and precipitation microphysics processes during the mature stage of Ianos are clearly evidenced by the analysis of both passive and active MW sensors onboard GPM-CO. Around the eye, in the northern side of the inner rainband, the GMI TB signature evidences the presence of shallow precipitation and warm rain processes, while in the rain bands the TBs evidence the presence of precipitation originating in the ice phase. The limited TB depression at 89 GHz corresponds to a substantial absence of large high-density frozen hydrometeors (i.e. graupel) in the upper levels. This behavior is often found in tropical cyclones, as reported for example by Cecil and Zipser, (1999) who carried out a study on the relationship between tropical cyclone intensity and satellite-based indicators of inner core convection, essentially derived from 85 GHz scattering signature and lightning activity. The authors point out that the 85 GHz TB (or PCT) is physically linked to the updraft strength, in that a depressed TB requires large ice aloft, which in turn requires a significant amount of vertical mass flux and latent heat release in the production of the ice. Similarly, lightning appears to require a combination of large and small ice particles together with supercooled liquid water. As a matter of fact, lightning occurrence is often very well correlated to strong TB (or PCT) depression at 85/89 GHz (i.e. Marra et al., 2017, 2019). While it is plausible that both of these observables should be related to the intensity of the medicane in some way, Cecil and Zipser (1999) rarely detect extreme ice-scattering signatures associated with strong updrafts and large graupel in tropical cyclones at their maximum intensity. The authors actually found higher correlations between inner core ice-scattering signatures (and lightning activity) and future intensity than between ice-scattering signatures and present intensity. Studies on hurricanes using flight-level measurements and vertically pointing Doppler radar (Black and Hallett, 1999) found general hurricane updrafts a factor of two weaker than continental updrafts. Typical values for mean vertical velocities in eyewall updrafts are 4 ms^{-1}, with maximum vertical velocities typically 7–8 ms^{-1}, and weaker in the rainbands. Similarly, at Ianos mature stage, no scattering signal (TB/PCT depression) is observed at 37 GHz remarking the presence of weak updrafts and sparse regions of supercooled drops and graupel growth. The graupel-ice electrification process in this case is unlikely because of the combined effect of strong horizontal wind, which contributes to carry away the ice particles, with the limited growth of graupel, not favoring the gravitational charge separation.

On the other hand, such conditions are evidently satisfied during Ianos development phase, when the GMI measurements show deep convection features with a marked TB or PCT depression at 89 GHz (PCT as low as 130 K). Significant PCT depression at 37 GHz (lowest values at 220 K) is also evident, highlighting the presence of strong updraft and solid-phase particles large enough to produce significant scattering at lower frequency. This behavior also finds correspondence with tropical cyclones, where vertical wind speeds at 20 ms^{-1} and many lightning discharges are observed when they are undergoing a rapid intensification phase (Black and Hallett, 1999). In such cases, the mixed-phase region extends at much higher altitudes, and large graupel is observed in the updraft just above the melting level. According to the findings of (Hourngir et al., 2021) using a 4-year GPM-CO observation dataset over the Mediterranean region to analyze deep convection, the minimum PCT values found for Ianos fall in the 1% coldest PCT values, both at 89 and 37 GHz of. This indicates that the deep convection features found during Ianos development phase are rarely observed, and could confirm the exceptional intensity of this storm. For example, (Marra et al., 2019) report the minimum GMI-based 89 GHz PCT during medicane Numa development phase 30 K higher with respect to Ianos. The GMI-based deep convection confirms what shown in earlier studies, it is deeper and more intense prior to the medicane maximum intensity (Claud et al., 2010; Miglietta et al., 2013), and that deep convection in the upshear quadrants leads to its intensification (Dafis et al., 2020) and transition to a tropical-like structure during the mature phase.

The GMI 166 GHz channels (TBs and polarization signal) show a comparable behavior during the two analyzed stages of Ianos highlighting significant TB depression not only in correspondence with the deep convective cores in the main rainband, but also in the surrounding areas mostly characterized by stratiform precipitation.

The DPR measurements available during Ianos mature phase have confirmed the features displayed by the GMI measurement analysis. A weak updraft strength in the convective regions of the inner rainband has been inferred from the 3D reflectivity (Z_{ku}) values and pattern. Both the maximum Z_{ku} as well as the Z_{ku} at near surface level rarely exceed 45 dBZ (a value typically found in presence of large hydrometeors), while the near-surface rainfall rate is generally lower than 50 mm h^{-1}. In addition, the DPR heavy ice flag (Iguchi et al., 2018) was found only in a few pixels. The storm top height does now exceed 12 km, but the maximum height for $Z_{ku} \geq 20$ dBZ was generally lower than 7 km with peaks around 9 km in correspondence of the convective cores. These values are significantly lower than those typically associated to deep convection, as shown in (Hourngir et al., 2021), where $\geq$20 dBZ echo top height approaches (or exceeds in case of overshooting tops) the tropopause. At the Ianos mature stage, the storm top height appears to be below the tropopause. According to the WMO tropopause definition

(i.e. the lowest level where the vertical temperature lapse rate is higher than -2 K km^{-1}), during Ianos mature phase it is between 14 and 16 km in proximity of the cyclone center, clearly indicating the warm core anomaly, as opposed to the 12 km during the development phase (not shown). This result is in contrast with the analysis of (Lagouvardos et al., 2021) based on the water vapour and infrared channel difference (WV-IR) method (Schmetz et al., 2002) used for the identification of deep convection and overshooting tops (Dafis et al., 2018). It has to be highlighted that the WV-IR method, although could be a good indicator of opaque clouds and convection, could lead to false detection of clouds approaching the tropopause (or overshooting top clouds) (Bedka et al., 2010). The lack of 40 dBZ reflectivity around the −10 °C level (at this level Z_{Ku} is generally lower than 30 dBZ with a peak at 37.5 dBZ), considered a characteristic of lightning-producing storms, according to Zipser and Lutz (1994) confirms the lack of large graupel particles in the charging zone as inferred from the GMI measurement analysis. DPR Ku-band reflectivity profiles also evidence an increasing bright-band height moving towards the medicane eye, indicating the presence of the warm core anomaly typical of the medicane mature phase. The DPR microphysics products reveal details on precipitation formation processes. Collisional break-up appears to be the dominant process in the convective regions, while in the stratiform regions (with embedded convection), in the outer rainbands, coalescence is the main precipitation formation process.

5. Conclusions

The goal of the present work is to exploit the satellite measurements from the NASA/JAXA GPM-CO active and passive MW sensors to analyze the precipitation structure of Medicane Ianos, the most intense tropical-like cyclone on record, which occurred in the Mediterranean Sea between 14 and 18 September 2020. Two GPM-CO overpasses are analyzed, one capturing Ianos at its development stage and one at its mature stage. The GMI measurements are used to carry out a comparative analysis of the medicane rainband structure and to infer precipitation microphysics and processes between the two phases. The DPR overpass, capturing for the first time ever the medicane during its mature phase, provides key measurements and products to analyze the 3D rainband structure and to verify the main precipitation formation processes, including the occurrence and strength of convection, as inferred from the passive MW measurements. The LINET strokes registered during the storm evolution are used to relate the deep convection features derived from the GPM-CO measurements to cloud electrification processes.

The study shows that: 1) the multi-sensor and multi-channel analysis of GMI passive microwave measurements allows to clearly identify different precipitation structure and processes, as well as different deep convection characteristics, in the development and in the mature stage; 2) the DPR offers extremely valuable products to analyze 3D precipitation microphysics, and convection strength, offering further evidence of the unique capabilities of GMI measurement for medicanes' structure and processes diagnostics; 3) the GPM-CO measurements provide evidence of tropical-like characteristics during Ianos mature phase, and of the exceptional intensity of this medicane; 4) the GPM-CO contributes to shed light on the different microphysics and dynamics processes connected to the cloud electrification mechanisms resulting in the electrically active (development) and weak (mature) Ianos phases.

This study demonstrates that with the advent of the GPM mission, with nearly-coincident measurements from the most advanced passive microwave radiometer in space, and from the first spaceborne precipitation radar covering the Mediterranean area, it is now possible not only to characterize medicanes' precipitation structure and microphysics processes with unprecedented detail, but also to provide evidence of similarities between exceptionally intense medicanes, such as Ianos, and tropical cyclones. Some recent studies, using both regional (Romera et al., 2017) and general circulation (González-Alemán et al., 2019) models have shown as the climate and the anthropogenic climate change in action seems to lead to a decrease in number of medicanes coupled with an increase of their intensity. In this frame, it is desirable to extend and achieve better satellite coverage to better characterize these phenomena.

CRediT authorship contribution statement

Leo Pio D'Adderio: Conceptualization, Methodology, Software, Writing – original draft, Writing – review & editing. **Daniele Casella:** Investigation, Writing – review & editing. **Stefano Dietrich:** Supervision. **Paolo Sanò:** Investigation, Writing – review & editing. **Giulia Panegrossi:** Data curation, Writing – original draft, Writing – review & editing, Supervision.

Declaration of Competing Interest

The authors declare that they have no known competing financial interests or personal relationships that could have appeared to influence the work reported in this paper.

Acknowledgments

This research was supported by the EUMETSAT Satellite Application Facility for Hydrology and Water Management (H SAF) Third Continuous Development and Operation Phase (CDOP-3). This article was partially based upon work from COST Action CA19109 MedCyclones; European Network for Mediterranean Cyclones in weather and climate, supported by COST-European Cooperation in Science and Technology (www.cost.eu). The efforts from the NASA Precipitation Processing System (PPS) data archive is gratefully acknowledged for hosting and making the GPM GMI and DPR products freely available. LINET data are provided by Nowcast GmhB (https://www.nowcast.de/) at CNR ISAC-Rome. The authors express their sincere gratitude to Dr. Stefano Federico for the fruitful scientific discussions and interactions during this work and to the two anonymous reviewers for their very useful comments and suggestions.

References

Bedka, K., Brunner, J., Dworak, R., Feltz, W., Otkin, J., Greenwald, T., 2010. Objective Satellite-based Detection of Overshooting Tops using infrared Window Channel Brightness Temperature Gradients. J. Appl. Meteorol. Climatol. 49, 181–202. https://doi.org/10.1175/2009JAMC2286.1.

Betz, H.-D., Schmidt, K., Oettinger, P., Wirz, M., 2004. Lightning detection with 3-D discrimination of intracloud and cloud-to-ground discharges: LIGHTNING DETECTION WITH 3-D MODE. Geophys. Res. Lett. 31, n/a-n/a. https://doi.org/10.1029/2004GL019821.

Betz, H.-D., Schmidt, K., Fuchs, B., Oettinger, W.P., Holler, H., 2007. Cloud lightning: detection and utilization for total lightning measured in the VLF/LF regime. J. Light. Res. 2, 1–17.

Black, R.A., Hallett, J., 1999. Electrification of the Hurricane. J. Atmos. Sci. 56, 2004–2028. https://doi.org/10.1175/1520-0469(1999)056<2004:EOTH>2.0.CO;2.

Carrió, D.S., Homar, V., Jansa, A., Romero, R., Picornell, M.A., 2017. Tropicalization process of the 7 November 2014 Mediterranean cyclone: numerical sensitivity study. Atmos. Res. 197, 300–312. https://doi.org/10.1016/j.atmosres.2017.07.018.

Cavicchia, L., von Storch, H., Gualdi, S., 2014. A long-term climatology of medicanes. Clim. Dyn. 43, 1183–1195. https://doi.org/10.1007/s00382-013-1893-7.

Cecil, D.J., Chronis, T., 2018. Polarization-corrected temperatures for 10-, 19-, 37-, and 89-GHz passive microwave frequencies. J. Appl. Meteorol. Climatol. 57, 2249–2265. https://doi.org/10.1175/JAMC-D-18-0022.1.

Cecil, D.J., Zipser, E.J., 1999. Relationships between tropical cyclone intensity and satellite-based indicators of inner core convection: 85-GHz ice-scattering signature and lightning. Mon. Weather Rev. 127, 103–123. https://doi.org/10.1175/1520-0493(1999)127<0103:RBTCIA>2.0.CO;2.

Cioni, G., Malguzzi, P., Buzzi, A., 2016. Thermal structure and dynamical precursor of a Mediterranean tropical-like cyclone: thermal Structure and Precursor of a MTLC. Q. J. R. Meteorol. Soc. 142, 1757–1766. https://doi.org/10.1002/qj.2773.

Claud, C., Alhammoud, B., Funatsu, B.M., Chaboureau, J.-P., 2010. Mediterranean hurricanes: large-scale environment and convective and precipitating areas from satellite microwave observations. Nat. Hazards Earth Syst. Sci. 10, 2199–2213. https://doi.org/10.5194/nhess-10-2199-2010.

Comellas Prat, A., Federico, S., Torcasio, R.C., D'Adderio, L.P., Dietrich, S., Panegrossi, G., 2021. Evaluation of the sensitivity of medicane ianos to model microphysics and initial conditions using satellite measurements. Remote Sens. 13, 4984. https://doi.org/10.3390/rs13244984.

D'Adderio, L.P., Porcù, F., Tokay, A., 2018. Evolution of drop size distribution in natural rain. Atmos. Res. 200, 70–76. https://doi.org/10.1016/j.atmosres.2017.10.003.

Dafis, S., Rysman, J., Claud, C., Flaounas, E., 2018. Remote sensing of deep convection within a tropical-like cyclone over the Mediterranean Sea. Atmos. Sci. Lett. 19 https://doi.org/10.1002/asl.823.

Dafis, S., Claud, C., Kotroni, V., Lagouvardos, K., Rysman, J., 2020. Insights into the convective evolution of Mediterranean tropical-like cyclones. Q. J. R. Meteorol. Soc. 146, 4147–4169. https://doi.org/10.1002/qj.3896.

Davis, C.A., Bosart, F., 2004. The TT problem: forecasting the tropical transition of cyclones. Bull. Am. Meteorol. Soc. 85, 1656–1662. https://doi.org/10.1175/BAMS-85-11-1657.

Davolio, S., Miglietta, M.M., Moscatello, A., Pacifico, F., Buzzi, A., Rotunno, R., 2009. Numerical forecast and analysis of a tropical-like cyclone in the Ionian Sea. Nat. Hazards Earth Syst. Sci. 9, 551–562. https://doi.org/10.5194/nhess-9-551-2009.

Draper, D.W., Newell, D.A., Wentz, F.J., Krimchansky, S., Skofronick-Jackson, G.M., 2015. The Global Precipitation Measurement (GPM) Microwave Imager (GMI): instrument overview and early on-orbit Performance. IEEE J. Sel. Top. Appl. Earth Obs. Remote Sens. 8, 3452–3462. https://doi.org/10.1109/JSTARS.2015.2403303.

Emanuel, 1986. An air-sea interaction theory for tropical cyclones. Part I: steady-state maintenance. Cover J. Atmos. Sci. J. Atmos. Sci. 43, 585–605. https://doi.org/10.1175/1520-0469(1986)043<0585:AASITF>2.0.CO;2.

Emanuel, K., 2005. Genesis and maintenance of "Mediterranean hurricanes". Adv. Geosci. 2, 217–220. https://doi.org/10.5194/adgeo-2-217-2005.

Fita, L., Flaounas, E., 2018. Medicanes as subtropical cyclones: the December 2005 case from the perspective of surface pressure tendency diagnostics and atmospheric water budget. Q. J. R. Meteorol. Soc. 144, 1028–1044. https://doi.org/10.1002/qj.3273.

Fita, Ll, Romero, R., Ramis, C., 2006. Intercomparison of intense cyclogenesis events over the Mediterranean basin based on baroclinic and diabatic influences. Adv. Geosci. 7, 333–342. https://doi.org/10.5194/adgeo-7-333-2006.

Flaounas, E., Gray, S.L., Teubler, F., 2021. A process-based anatomy of Mediterranean cyclones: from baroclinic lows to tropical-like systems. Weather Clim. Dyn. 2, 255–279. https://doi.org/10.5194/wcd-2-255-2021.

Formenton, M., Panegrossi, G., Casella, D., Dietrich, S., Mugnai, A., Sanò, P., Di Paola, F., Betz, H.-D., Price, C., Yair, Y., 2013. Using a cloud electrification model to study relationships between lightning activity and cloud microphysical structure. Nat. Hazards Earth Syst. Sci. 13, 1085–1104. https://doi.org/10.5194/nhess-13-1085-2013.

Gong, J., Wu, D.L., 2017. Microphysical properties of frozen particles inferred from Global Precipitation Measurement (GPM) Microwave Imager (GMI) polarimetric measurements. Atmos. Chem. Phys. 17, 2741–2757. https://doi.org/10.5194/acp-17-2741-2017.

González-Alemán, J.J., Pascale, S., Gutierrez-Fernandez, J., Murakami, H., Gaertner, M. A., Vecchi, G.A., 2019. Potential increase in Hazard from Mediterranean hurricane activity with global warming. Geophys. Res. Lett. 46, 1754–1764. https://doi.org/10.1029/2018GL081253.

Grecu, M., Olson, W.S., Munchak, S.J., Ringerud, S., Liao, L., Haddad, Z., Kelley, B.L., McLaughlin, S.F., 2016. The GPM combined algorithm. J. Atmos. Ocean. Technol. 33, 2225–2245. https://doi.org/10.1175/JTECH-D-16-0019.1.

Hersbach, H., Bell, B., Berrisford, P., Hirahara, S., Horányi, A., Muñoz-Sabater, J., Nicolas, J., Peubey, C., Radu, R., Schepers, D., Simmons, A., Soci, C., Abdalla, S., Abellan, X., Balsamo, G., Bechtold, P., Biavati, G., Bidlot, J., Bonavita, M., Chiara, G., Dahlgren, P., Dee, D., Diamantakis, M., Dragani, R., Flemming, J., Forbes, R., Fuentes, M., Geer, A., Haimberger, L., Healy, S., Hogan, R.J., Hólm, E., Janisková, M., Keeley, S., Laloyaux, P., Lopez, P., Lupu, C., Radnoti, G., Rosnay, P., Rozum, I., Vamborg, F., Villaume, S., Thépaut, J., 2020. The ERA5 global reanalysis. Q. J. R. Meteorol. Soc. 146, 1999–2049. https://doi.org/10.1002/qj.3803.

Hou, A.Y., Kakar, R.K., Neeck, S., Azarbarzin, A.A., Kummerow, C.D., Kojima, M., Oki, R., Nakamura, K., Iguchi, T., 2014. The global precipitation measurement mission. Bull. Am. Meteorol. Soc. 95, 701–722. https://doi.org/10.1175/BAMS-D-13-00164.1.

Hourngir, D., Panegrossi, G., Casella, D., Sanò, P., D'Adderio, L.P., Liu, C., 2021. A 4-year climatological analysis based on GPM observations of deep convective events in the Mediterranean Region. Remote Sens. 13, 1685. https://doi.org/10.3390/rs13091685.

Iguchi, T., Kawamoto, N., Oki, R., 2018. Detection of intense Ice precipitation with GPM/DPR. J. Atmos. Ocean. Technol. 35, 491–502. https://doi.org/10.1175/JTECH-D-17-0120.1.

Lagouvardos, K., Kotroni, V., Nickovic, S., Jovic, D., Kallos, G., Tremback, C.J., 1999. Observations and model simulations of a winter sub-synoptic vortex over the Central Mediterranean. Met. Apps 6, 371–383. https://doi.org/10.1017/S1350482799001309.

Lagouvardos, K., Karagiannidis, A., Dafis, S., Kalimeris, A., Kotroni, V., 2021. Ianos - a hurricane in the Mediterranean. Bull. Am. Meteorol. Soc. 1–31 https://doi.org/10.1175/BAMS-D-20-0274.1.

Marra, A.C., Porcù, F., Baldini, L., Petracca, M., Casella, D., Dietrich, S., Mugnai, A., Sanò, P., Vulpiani, G., Panegrossi, G., 2017. Observational analysis of an exceptionally intense hailstorm over the Mediterranean area: role of the GPM Core observatory. Atmos. Res. 192, 72–90. https://doi.org/10.1016/j.atmosres.2017.03.019.

Marra, A.C., Federico, S., Montopoli, M., Avolio, E., Baldini, L., Casella, D., D'Adderio, L. P., Dietrich, S., Sanò, P., Torcasio, R.C., Panegrossi, G., 2019. The precipitation structure of the Mediterranean tropical-like cyclone numa: analysis of GPM observations and numerical weather prediction model simulations. Remote Sens. 11, 1690. https://doi.org/10.3390/rs11141690.

Mazza, E., Ulbrich, U., Klein, R., 2017. The tropical transition of the October 1996 medicane in the Western Mediterranean Sea: a warm seclusion event. Mon. Weather Rev. 145, 2575–2595. https://doi.org/10.1175/MWR-D-16-0474.1.

Michaelides, S., Karacostas, T., Sánchez, J.L., Retalis, A., Pytharoulis, I., Homar, V., Romero, R., Zanis, P., Giannakopoulos, C., Bühl, J., Ansmann, A., Merino, A., Melcón, P., Lagouvardos, K., Kotroni, V., Bruggeman, A., López-Moreno, J.I., Berthet, C., Katragkou, E., Tymvios, F., Hadjimitsis, D.G., Mamouri, R.-E., Nisantzi, A., 2018. Reviews and perspectives of high impact atmospheric processes in the Mediterranean. Atmos. Res. 208, 4–44. https://doi.org/10.1016/j.atmosres.2017.11.022.

Miglietta, M.M., Rotunno, R., 2019. Development mechanisms for Mediterranean tropical-like cyclones (medicanes). Q. J. R. Meteorol. Soc. 145, 1444–1460. https://doi.org/10.1002/qj.3503.

Miglietta, M.M., Moscatello, A., Conte, D., Mannarini, G., Lacorata, G., Rotunno, R., 2011. Numerical analysis of a Mediterranean 'hurricane' over South-Eastern Italy: sensitivity experiments to sea surface temperature. Atmos. Res. 101, 412–426. https://doi.org/10.1016/j.atmosres.2011.04.006.

Miglietta, M.M., Laviola, S., Malvaldi, A., Conte, D., Levizzani, V., Price, C., 2013. Analysis of tropical-like cyclones over the Mediterranean Sea through a combined modeling and satellite approach: TLC analysis through a combined approach. Geophys. Res. Lett. 40, 2400–2405. https://doi.org/10.1002/grl.50432.

Miglietta, M.M., Mastrangelo, D., Conte, D., 2015. Influence of physics parameterization schemes on the simulation of a tropical-like cyclone in the Mediterranean Sea. Atmos. Res. 153, 360–375. https://doi.org/10.1016/j.atmosres.2014.09.008.

Miglietta, M.M., Cerrai, D., Laviola, S., Cattani, E., Levizzani, V., 2017. Potential vorticity patterns in Mediterranean "hurricanes". Geophys. Res. Lett. 44, 2537–2545. https://doi.org/10.1002/2017GL072670.

Moscatello, A., Miglietta, M.M., Rotunno, R., 2008. Numerical analysis of a Mediterranean "Hurricane" over Southeastern Italy. Mon. Weather Rev. 136, 4373–4397. https://doi.org/10.1175/2008MWR2512.1.

Nastos, P.T., Karavana Papadimou, K., Matsangouras, I.T., 2018. Mediterranean tropical-like cyclones: Impacts and composite daily means and anomalies of synoptic patterns. Atmos. Res. 208, 156–166. https://doi.org/10.1016/j.atmosres.2017.10.023.

Panegrossi, G., Casella, D., Dietrich, S., Marra, A.C., Sano, P., Mugnai, A., Baldini, L., Roberto, N., Adirosi, E., Cremonini, R., Bechini, R., Vulpiani, G., Petracca, M., Porcu, F., 2016. Use of the GPM constellation for monitoring heavy precipitation events over the Mediterranean Region. IEEE J. Sel. Top. Appl. Earth Obs. Remote Sens. 9, 2733–2753. https://doi.org/10.1109/JSTARS.2016.2520660.

Panegrossi, G., Rysman, J.-F., Casella, D., Marra, A., Sanò, P., Kulie, M., 2017. CloudSat-Based Assessment of GPM Microwave Imager Snowfall Observation Capabilities. Remote Sens. 9, 1263. https://doi.org/10.3390/rs9121263.

Panegrossi, G., Marra, A.C., Sanò, P., Baldini, L., Casella, D., Porcù, F., 2020. Heavy precipitation systems in the Mediterranean area: the role of GPM. In: Levizzani, V., Kidd, C., Kirschbaum, D.B., Kummerow, C.D., Nakamura, K., Turk, F.J. (Eds.), Satellite Precipitation Measurement, Advances in Global Change Research. Springer International Publishing, Cham, pp. 819–841. https://doi.org/10.1007/978-3-030-35798-6_18.

Picornell, M.A., Campins, J., Jansà, A., 2014. Detection and thermal description of medicanes from numerical simulation. Nat. Hazards Earth Syst. Sci. 14, 1059–1070. https://doi.org/10.5194/nhess-14-1059-2014.

Pytharoulis, I., Craig, G.C., Ballard, S.P., 1999. Study of the Hurricane-like Mediterranean cyclone of January 1995. Phys. Chem. Earth Part B 24, 627–632. https://doi.org/10.1016/S1464-1909(99)00056-8.

Ragone, F., Mariotti, M., Parodi, A., von Hardenberg, J., Pasquero, C., 2018. A climatological study of Western Mediterranean Medicanes in numerical simulations with explicit and parameterized convection. Atmosphere 9, 397. https://doi.org/10.3390/atmos9100397.

Reale, Atlas, 2001. Tropical cyclone–like vortices in the extratropics: observational evidence and synoptic analysis. Weather Forecast. 16, 7–34. https://doi.org/10.1175/1520-0434(2001)016<0007:TCLVIT>2.0.CO;2.

Romera, R., Gaertner, M.Á., Sánchez, E., Domínguez, M., González-Alemán, J.J., Miglietta, M.M., 2017. Climate change projections of medicanes with a large multi-model ensemble of regional climate models. Glob. Planet. Chang. 151, 134–143. https://doi.org/10.1016/j.gloplacha.2016.10.008.

Schmetz, J., Pili, P., Tjemkes, S., Just, D., Kerkmann, J., Rota, S., Ratier, A., 2002. Supplement to an Introduction to Meteosat Second Generation (MSG): SEVIRI CALIBRATION. Bull. Am. Meteor. Soc. 83, 992. https://doi.org/10.1175/BAMS-83-7-Schmetz-2.

Seto, S., Iguchi, T., Oki, T., 2013. The basic performance of a precipitation retrieval algorithm for the global precipitation measurement mission's single/dual-frequency radar measurements. IEEE Trans. Geosci. Remote Sens. 51, 5239–5251. https://doi.org/10.1109/TGRS.2012.2231686.

Skofronick-Jackson, G., Petersen, W.A., Berg, W., Kidd, C., Stocker, E.F., Kirschbaum, D. B., Kakar, R., Braun, S.A., Huffman, G.J., Iguchi, T., Kirstetter, P.E., Kummerow, C., Meneghini, R., Oki, R., Olson, W.S., Takayabu, Y.N., Furukawa, K., Wilheit, T., 2017. The Global Precipitation Measurement (GPM) mission for science and society. Bull. Am. Meteorol. Soc. 98, 1679–1695. https://doi.org/10.1175/BAMS-D-15-00306.1.

Spencer, R.W., Goodman, H.M., Hood, R.E., 1989. Precipitation retrieval over land and ocean with the SSM/I: identification and characteristics of the scattering signal. J. Atmos. Ocean. Technol. 6, 254–273. https://doi.org/10.1175/1520-0426(1989)006<0254:PROLAO>2.0.CO;2.

Willis, P.T., Hallett, J., Black, R.A., Hendricks, W., 1994. An aircraft study of rapid precipitation development and electrification in a growing convective cloud. Atmos. Res. 33, 1–24. https://doi.org/10.1016/0169-8095(94)90010-8.

Zalachoris, G., 2020. The September 18–20 2020 Medicane Ionos Impact on Greece. https://doi.org/10.18118/G6MT1T.

Zhang, W., Zhang, Y., Zheng, D., Zhou, X., 2012. Lightning distribution and eyewall outbreaks in tropical cyclones during landfall. Mon. Weather Rev. 140, 3573–3586. https://doi.org/10.1175/MWR-D-11-00347.1.

Zipser, E.J., Lutz, K.R., 1994. The vertical profile of radar reflectivity of convective cells: a strong indicator of storm intensity and lightning probability? Mon. Weather Rev. 122, 1751–1759. https://doi.org/10.1175/1520-0493(1994)122<1751:TVPORR>2.0.CO;2.